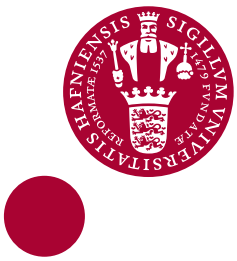

The age of surface-exposed ice along the northern margin of the Greenland Ice Sheet

MacGregor, Joseph A.; Fahnestock, Mark A.; Colgan, William T.; Larsen, Nicolaj K.; Kjeldsen, Kristian K.; Welker, Jeffrey M.

Published in:
Journal of Glaciology

DOI:
10.1017/jog.2020.62

Publication date:
2020

Document version
Publisher's PDF, also known as Version of record

Journal of Glaciology

Article

Cite this article: MacGregor JA, Fahnestock MA, Colgan WT, Larsen NK, Kjeldsen KK, Welker JM (2020). The age of surface-exposed ice along the northern margin of the Greenland Ice Sheet. *Journal of Glaciology* **66**(258), 667–684. https://doi.org/10.1017/jog.2020.62

Received: 11 December 2019
Revised: 9 July 2020
Accepted: 9 July 2020

Key words:
Ice and climate; ice chronology/dating; paleoclimate; remote sensing

Author for correspondence:
Joseph A. MacGregor,
E-mail: joseph.a.macgregor@nasa.gov

The age of surface-exposed ice along the northern margin of the Greenland Ice Sheet

Joseph A. MacGregor[1], Mark A. Fahnestock[2], William T. Colgan[3], Nicolaj K. Larsen[4], Kristian K. Kjeldsen[3] and Jeffrey M. Welker[5,6]

[1]Cryospheric Sciences Laboratory, NASA Goddard Space Flight Center, Greenbelt, Maryland, USA; [2]Geophysical Institute, University of Alaska Fairbanks, Fairbanks, Alaska, USA; [3]Geological Survey of Denmark and Greenland, Copenhagen, Denmark; [4]Section for GeoGenetics, Globe Institute, University of Copenhagen, Copenhagen, Denmark; [5]Department of Biological Sciences, University of Alaska Anchorage, Anchorage, Alaska, USA and [6]Department of Ecology and Genetics, University of Oulu, Oulu, Finland

Abstract

Each summer, surface melting of the margin of the Greenland Ice Sheet exposes a distinctive visible stratigraphy that is related to past variability in subaerial dust deposition across the accumulation zone and subsequent ice flow toward the margin. Here we map this surface stratigraphy along the northern margin of the ice sheet using mosaicked Sentinel-2 multispectral satellite imagery from the end of the 2019 melt season and finer-resolution WorldView-2/3 imagery for smaller regions of interest. We trace three distinct transitions in apparent dust concentration and the top of a darker basal layer. The three dust transitions have been identified previously as representing late-Pleistocene climatic transitions, allowing us to develop a coarse margin chronostratigraphy for northern Greenland. Substantial folding of late-Pleistocene stratigraphy is observed but uncommon. The oldest conformal surface-exposed ice in northern Greenland is likely located adjacent to Warming Land and may be up to ~55 thousand years old. Basal ice is commonly exposed hundreds of metres from the ice margin and may indicate a widespread frozen basal thermal state. We conclude that the ice margin across northern Greenland offers multiple opportunities to recover paleoclimatically distinct ice relative to previously studied regions in southwestern Greenland.

1. Introduction

Bare ice is exposed subaerially along the margin of the Greenland Ice Sheet (GrIS) for a period of weeks to months each boreal summer, after the previous year's snowfall has melted entirely (Fahnestock and others, 1993). This region – the ablation zone – presently includes more than 12% of the ice sheet by surface area (McGrath and others, 2013). The ablation zone is predicted to expand given continued anthropogenic climate warming, and indeed such an expansion was recently reported and is particularly acute for northern Greenland (Noël and others, 2019). Given downward advection of ice in the accumulation zone and upward advection in the ablation zone, the oldest subaerially exposed surface of an ice mass is generally found along the ice margin, in the ablation zone of land-terminating ice (Hooke, 2020).

Subaerial exposure of ice from the late Pleistocene epoch was first documented in the ablation zone of the Barnes Ice Cap on Baffin Island by Hooke (1976). There, Pleistocene ice was distinctly whiter than more recent, bluer Holocene ice. Consistent with ice-core records, the stable oxygen-isotope fractionation ratio ($\delta^{18}O$) of candidate Pleistocene ice was also depleted significantly relative to Holocene ice. For Greenland, between 1985 and 1994 (all years Common Era), Niels Reeh and several collaborators sampled surface ice within the GrIS ablation zone and measured its $\delta^{18}O$ value. Their goal was to identify sites with inexpensive access to paleoclimatically distinct ice from the late Pleistocene and Holocene epochs (Reeh and others, 2002 and references therein; hereafter R02; Fig. 1). That work resulted in a breakthrough for a bulk sampling of paleo-atmospheres, which has since been exploited regularly in Greenland and elsewhere (e.g. Petrenko and others, 2006; Aciego and others, 2007; Schaefer and others, 2009; Kurbatov and others, 2010), and it also informed correlation of surface-intersecting internal radiostratigraphy with surface-exposed visible stratigraphy (Kjær and others, 2018).

As a result of their sampling campaign, R02 identified a visually distinctive surface stratigraphy along the GrIS margin that enables a broad age classification of exposed ice from the late Pleistocene (~129–11.7 ka, where 'ka' means thousands of years ago) and Holocene (11.7–0 ka) epochs. Within the late Pleistocene, this classification includes recent major climate transitions within the Last Glacial Period (LGP; ~115–11.7 ka): the Younger Dryas (YD, 12.8–11.7 ka) stadial, Bølling–Allerød (B–A, 14.7–12.8 ka) interstadial and pre-B-A portion of the LGP (115–14.7 ka) (Rasmussen and others, 2006). This surface stratigraphy is due to spatiotemporal variability in several factors, including the dust concentration in subaerially deposited snow at the time of burial, and the rates of downward vertical advection (burial) in the upstream dry snow zone, horizontal ice flow and upward advection (emergence) in the ablation zone (e.g. Bøggild and others, 1996, 2010; Wientjes and others, 2012).

In recent years, multiple new satellite-borne multispectral sensors have been launched that can reliably detect ablation-zone surface stratigraphy during the melt season with a metre to

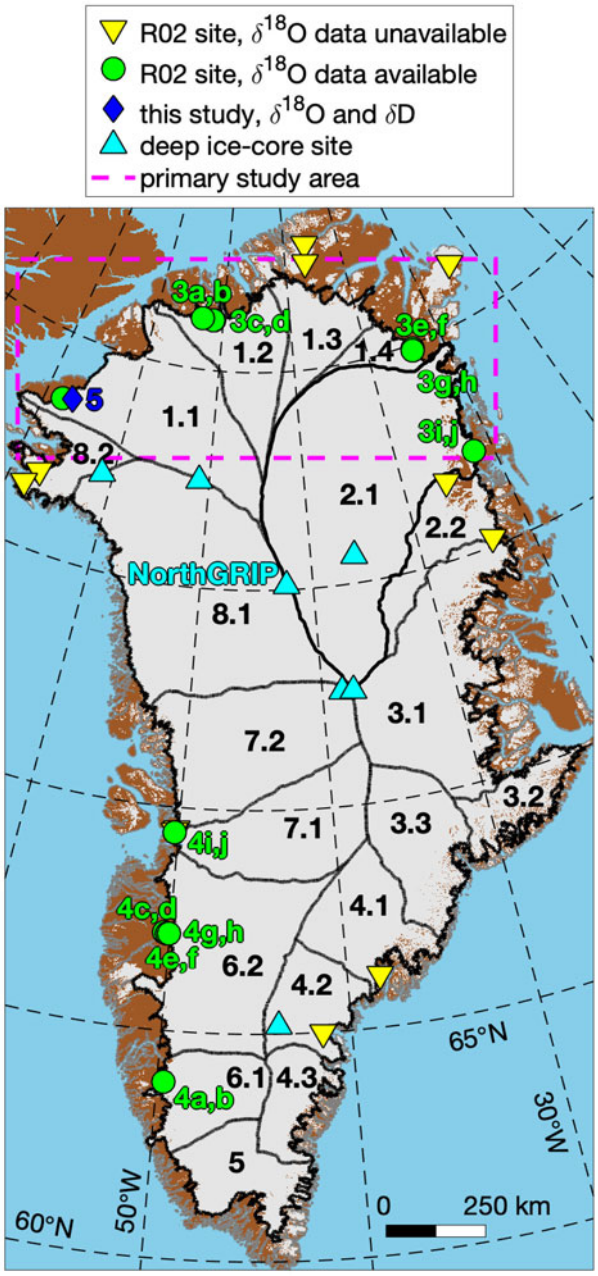

Fig. 1. Map of Greenland identifying all $\delta^{18}O$ surface-sampling sites reported by R02, including the subset for which $\delta^{18}O$ data are available and the new Hiawatha Glacier site reported by this study. Green site labels denote figure numbers/panels where each site is further examined. Black numbers denote primary ice-sheet drainage systems (Zwally and others, 2012).

decametre resolution. Here we use Sentinel-2A/B (S2) and WorldView-2/3 (WV) satellite imagery to map the large-scale chronostratigraphy of the northern GrIS margin. We contextualise existing and new in situ $\delta^{18}O$ measurements to evaluate correlations between surface-ice brightness/colour and isotopic composition (and hence apparent ice age). We identify key stratigraphic features of interest, including the apparent location of what is likely the oldest coherent surface-exposed ice in northern Greenland, the geographic pattern of basal ice exposures in northern Greenland and its potential implications for the basal thermal state there.

2. Data and methods

2.1. Satellite imagery and derived products

Sentinel-2A was launched by the European Space Agency (ESA) in 2015 as a continuation of decades-long international efforts to map global land change, and its twin Sentinel-2B followed in 2017. Their multispectral visible-wavelength sensors have a fine radiometric resolution (12-bit), similar to Landsat-8, enabling reliable detection of subtle changes in surface reflectance at a 10-m spatial resolution regularly (e.g. Fahnestock and others, 2016; Yang and others, 2019). While multiple other high-sensitivity visible-wavelength multispectral sensors now exist, including Landsat-8 and the WV constellation, we opted to primarily use S2 imagery for the examination of the GrIS surface stratigraphy. This selection was made because it combined moderate spatial resolution, which simplifies the production of an ice-sheet-wide mosaic, wide across-track swath, frequent revisits during the melt season (effectively ~5-d repeat with both satellites operational), and data availability within our selected processing platform (Google Earth Engine; Gorelick and others, 2017).

Since the beginning of S2 operations in mid-2015, the GrIS experienced its most widespread surface melting during the summer of 2019, due to a large high-pressure atmospheric anomaly (Tedesco and Fettweis, 2020). While the major surface chronostratigraphic boundaries are typically within 5 km of the ice margin and are visible at the end of most summer melt seasons, the extensive 2019 melt season provided an opportunity to image a larger expanse of bare ice for an extended period. We leverage this extended exposure of surface ice in the north by constructing a full-resolution mosaic of Greenland based on S2 imagery from August 2019 only.

Within Google Earth Engine, we identify all S2 scenes collected over Greenland in August of 2019 with a reported cloud-cover fraction of ⩽15%. We use Level-1C S2 scenes (orthorectified, top-of-atmosphere reflectance), which have a pixel-scale geolocation uncertainty that is acceptable for the substantially larger scales of interest in our study. We then define a 10-m grid across Greenland and overlay all available individual scenes, and record the median value of the red, green and blue channels (4, 3 and 2, respectively) of those scenes in each grid cell to generate the mosaic. We then apply a gamma correction with a value of 1.5 to enhance low-end contrast. No additional filtering is performed. While the data volumes we analyse remotely are large, our processing chain is simple, with the goal of generating a mosaic of direct value for detecting and mapping surface stratigraphy along the ice margin.

For portions of the ice-sheet margin where R02 sampled between 1985 and 1994 (Fig. 1), or where the surface stratigraphy in S2 imagery appears either particularly complex or anomalous, we also examine with WV 1.24–2.4-m nadir-resolution 11-bit multispectral imagery. As for the S2 imagery, we examine the red, green and blue channels only (5, 3 and 2, respectively) of orthorectified WV images that also have a pixel-scale geolocation uncertainty. This imagery is either from July or August in the most recent available year (2013–2018) and is not contemporaneous with the 2019 S2 mosaic. Although this time difference (up to 6 years) is a potential source of ambiguity for interpretation, this effect is expected to be minor given slow to negligible ice flow within 5 km of the mostly stable portion of the GrIS margin that is land-terminating.

We use two additional higher-level satellite-derived products to facilitate our analysis. For the referencing traced layer extents to the ice margin, we vectorise the 15-m-resolution Greenland Ice Mapping Project (GIMP v1) ice mask (Howat and others, 2014; Howat, 2017), which was generated using Landsat-7 ETM + imagery from 1999 to 2002. This time difference between the GIMP v1 ice margin and our 2019 S2 mosaic (up to two decades) is large enough that potential margin migration warrants consideration, especially given independent knowledge of changes in GrIS configuration during this period (e.g. Kjeldsen and others, 2015). Excepting the southwestern sector of Humboldt Glacier,

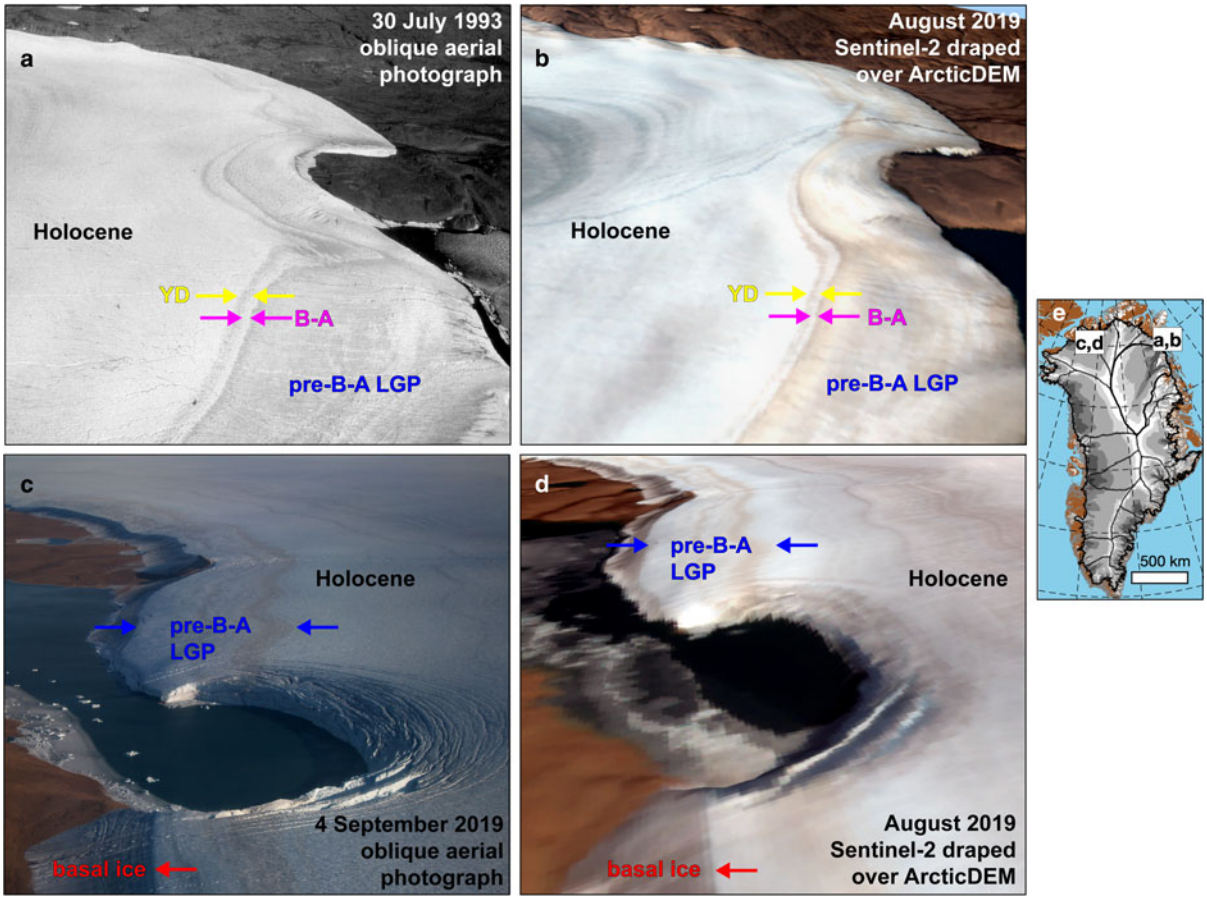

Fig. 2. (a) Oblique aerial photograph of GrIS margin taken 30 July 1993 from near the Kronprins Christian Land K site (Table 1) looking north–northeast (same as Fig. 2 of R02), with R02's original interpretation superimposed. Credit: H. Oerter. Reprinted from Annals of Glaciology with permission from the International Glaciology Society. (b) August 2019 S2 mosaic draped over 10-m ArcticDEM, with perspective and camera position oriented to approximately reproduce panel a and S2 colours contrast-stretched. No vertical exaggeration. (c) Oblique aerial photograph of GrIS margin adjacent to Daugaard-Jensen Land taken 4 September 2019 looking east–northeast, with age interpretation superimposed. Note that the YD and B-A layers are only faintly visible there and were not traced in the S2 mosaic. Credit: J. Sonntag. (d) Same as panel b, but for the site shown in panel c. (e) Map of Greenland showing the location of both sites, where greyscale is surface speed, as shown in Fig. 7. Contains Copernicus Sentinel-2 2019 data processed by ESA.

nearly all the margin stratigraphy we traced was across land-terminating ice. We occasionally observed margin migration – nearly invariably retreat – on the order of several S2 pixels (tens of metres), and this pattern seemed to be most common in the vicinity of small proglacial lakes. However, we did not retrace the ice margin of the northern GrIS, as we considered that task beyond the scope of this study. Therefore, we accept that this discrepancy may induce a small, spatially variable overestimation of the margin-perpendicular horizontal layer extents discussed below. For high-resolution surface elevations at sites of interest, we use the 10-m-resolution version of the ArcticDEM v7 mosaic, which has an effective time stamp similar to the WV imagery we used (Porter and others, 2018). We assume that ongoing rapid thinning of the northern margin of the GrIS does not significantly affect our use of ArcticDEM as a visual aid for this study (Smith and others, 2020*a*).

2.2. Stable isotope transects from surface ice

We base our interpretation of the surface chronostratigraphy of the ice-sheet margin on the correlation identified by R02 between surface optical brightness and $\delta^{18}O$ measurements of surface-exposed ice (where $\delta^{18}O$ is a measure of the isotopic fractionation of ^{18}O to ^{16}O, as compared to reference seawater). They hypothesised that patterns in surface brightness relate directly to the ice's age for multiple major climatic periods known to be preserved within the present-day GrIS. R02 supported this hypothesis with a single monochrome photograph depicting the ice-sheet margin in Kronprins Christian Land in northeastern Greenland (their Fig. 2; our Fig. 2a). R02 stated that '*Alternating light- and dark-coloured bands running parallel to the ice margin* are *visible. The wide dark band nearest to the ice edge* is *~1 km wide and* consists *of pre-Holocene ice. The thin light and dark bands adjacent to the wide dark band* are *the Bølling–Allerød/Younger Dryas climate oscillation. The light-coloured ice to the left* is *Holocene ice.*'

R02 did not directly georeference $\delta^{18}O$ values to that oblique aerial photograph, so it was not immediately clear how well this relation holds there or elsewhere, but Bøggild and others (2010) reported the patterns of surface dust concentration from this site that were consistent with R02's hypothesis. The success of later studies of ice-sheet surface geochemistry elsewhere across the GrIS further suggests R02's hypothesised relation is generally valid for coarsely identifying ice of the desired age (e.g. Petrenko and others, 2006). Figure 2 shows unambiguously that the qualitative chronostratigraphic interpretation of R02 is reproducible using satellite imagery of Kronprins Christian Land and elsewhere in northern Greenland. Kjær and others (2018) also reproduced the R02 photograph synthetically in a similar manner, from which they further argued that this interpretation is also qualitatively consistent with internal radiostratigraphy where it intersects the ice surface.

In general, the exact positions of R02's surface $\delta^{18}O$ transects are not well known, likely because their collection predates the

widespread use of global navigation satellite systems (GNSSs). Further, the azimuths of the surface transects were neither reported nor described, so we assume that they were roughly margin-perpendicular and prescribe these values with a precision of 5° (Table 1). R02 recognised this ambiguity, as not all authors were present during each sampling effort, and they described each site qualitatively with varying degrees of detail. Here we use a database that contains both $\delta^{18}O$ values and along-transect distances for multiple R02 sites (H. Oerter, pers. comm., 2018). As needed, we translate the transect-origin locations manually with a precision of 10 m so that the most margin-proximal sample of each transect is at the ice-sheet margin (Table 1).

In one case (Inglefield Land), the given position is nearly 9 km away from the present ice-sheet margin, an ambiguity noted by R02. We determined an approximate translation for this site to a location that is roughly consistent with a photograph of a portion of the margin visited by Risbo and Pedersen (1994), who performed the sampling there. However, its location is too uncertain and the margin stratigraphy of this region is too complex to justify comparison of this $\delta^{18}O$ transect with modern satellite imagery. Hence, we do not further consider this R02 site.

In late July 2019, we collected one additional surface transect near the southwest corner of Hiawatha Glacier, adjacent to Inglefield Land (Fig. 1), to better understand the chronostratigraphy of this complex margin. Ice samples were collected in a manner similar to that described by R02, i.e. several centimetres of surface crust were removed with an ice axe, then the ice was chipped from the underlying solid surface and placed into 60-mL polypropylene bottles. We collected 84 samples with a mean separation of 9.5 m and sampling locations were recorded with a Geode™ mapping-grade GNSS receiver with sub-meter accuracy. The ice was then melted and both $\delta^{18}O$ and δD (^{2}H to ^{1}H isotopic ratio) values of the resulting meltwater were measured by a mass spectrometer at the University of Oulu.

2.3. Layer tracing

To map potential chronostratigraphic units (layers) within the S2 mosaic based on contrasts in apparent surface brightness and colour, we examined the ice-sheet margin within the mosaic at a 1: 10 000 scale in QGIS version 3. We used local contrast stretching to improve visual boundary identification (typically min./max. stretch to 2–98% cumulative count), and traced boundaries manually. Where such boundaries were ambiguous, we did not trace them. We briefly explored alternative automated tracing schemes, including spectral band ratios, to identify individual layers. However, such schemes were typically challenged by variable cloudiness, solar elevation angle and the quality of preliminary versions of the mosaic, so we consider further development thereof beyond the scope of the present study. Our manual tracing approach is somewhat analogous to that of MacGregor and others (2015), who traced GrIS radiostratigraphy semi-automatically. We sacrifice deeper investigation of methodological sophistication and automation, which may enable rapid scalability in the future, so that at first, large-scale evaluation of northern GrIS margin surface stratigraphy can be generated.

Here we focus primarily on the boundaries that separate the four layers identified visually or described by R02. While additional visually distinctive layers are observed that appear to originate from both within and before the Holocene, these layers are not as widespread across the northern GrIS, nor were they identified visually by R02, nor were candidates ages assigned to them by that study.

We next describe these four boundaries in their typical stratigraphic order from top (highest exposed and farthest from the margin) to bottom (lowest exposed, at or closest to the margin).

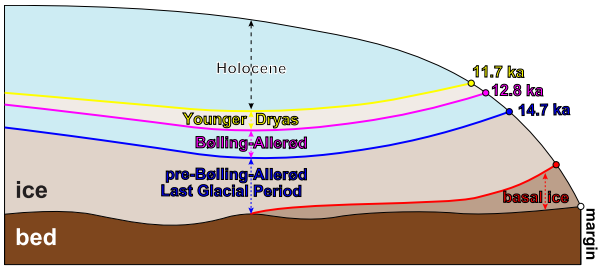

Fig. 3. Simplified cross-section of the margin of the northern GrIS illustrating the typical chronostratigraphy we mapped (circles). Boundary colours are the same as used for other figures. Not all boundaries were always detected, nor were they always found in this stratigraphic order due to occasional folding. Ice colour is exaggerated and approximates that which we observed following local contrast stretching when mapping boundaries at 1: 10 000 scale.

Figure 3 shows a simple ice-sheet cross-section illustrating these boundaries. The first boundary we traced is the bottom of the Holocene layer (i.e. its lowermost limit, 11.7 ka), which is identified by the characteristic sharp transition between white and light brown ice (Bøggild and others, 2010). The second is the bottom of the YD layer (12.8 ka), which directly underlies the Holocene layer, is typically a light brown colour and is relatively thin, i.e. the length of its margin-perpendicular horizontal exposure rarely exceeds ~200 m. This particular boundary is harder to trace because it is often less distinct than the others and it is closely sandwiched between the above Holocene boundary and the next meteoric boundary below it. The third boundary is the bottom of the B–A layer (14.7 ka), which is the bottom of the thin white layer that separates the dustier/browner YD layer above it from the darker brown pre-B-A LGP ice beneath it. Finally, we traced the upper boundary of what we assume is basal ice, which is significantly darker and greyer than the overlying Holocene or pre-Holocene ice and is typically not conformal to those meteoric strata. Hence, it has no specific age, although it typically underlies what appears to be pre-Holocene ice from within the LGP (115–11.7 ka). Tracing this boundary enables both better estimates of the horizontal length of surface-exposed pre-Holocene meteoric ice – rather than only using the ice margin – and also an opportunity to more broadly contextualise these basal ice exposures.

For WV imagery adjacent to Hiawatha Glacier and Warming Land, we retraced the four boundaries described above at finer scales (between 1:1000 and 1:2500), leveraging the finer resolution permitted by that imagery. For two locations adjacent to Warming Land, we also traced additional boundaries between alternating layers of whiter and browner ice in pre-B-A LGP ice that are not as distinct in the coarser-resolution S2 imagery.

To calculate plan-view distances between traced boundaries (the surface-exposed, horizontal layer thickness; not corrected for slope), we first determine the shortest distance between each digitised point and the ice margin or nunatak perimeter, whichever is closest. For each traced boundary, we then determine where each lower boundary (i.e. more margin-proximal) intersects the line that connects each of the upper boundaries' digitised points and the ice margin. In doing so, we approximate the margin-perpendicular horizontal exposure of each 'layer' (the stratigraphic unit between traced boundary pairs). All reported distances/thicknesses are great-circle arclengths on the surface of the WGS84 ellipsoid, not Cartesian distances within our default projection (EPSG:3413), which can differ by >2% at 80° N for the spatial scales we consider.

2.4 Ice-core data

To evaluate the apparent age of pre-B-A LGP ice, we use the NorthGRIP ice-core dust-concentration record produced by

Table 1. Geographic data and applied translations for R02 $\delta^{18}O$ surface transects

Figure 4/5 Panels	Reeh and others (2002) ice-sheet margin site	Latitude (°N)	Longitude (°W)	Transect azimuth (°)	Horizontal translation (m)	Translation azimuth (°)
4a, b	Warming Land 3	81.1721	53.1600	165	40	0
4a, b	Warming Land 4	81.1721	53.1311	145	50	330
4c, d	Warming Land 1	81.1565	51.4195	175	70	20
4c, d	Warming Land 2	81.1565	51.4661	185	100	170
4e, f	Kronprins Christian Land K	79.9084	24.0531	300	1080	110
4g, h	Kronprins Christian Land KS	79.8517	24.1747	290	530	110
4i, j	Storstrømmen N/NS	77.1865	22.0030	265	1360	285
5a, b	Isortuarssup	63.8724	49.6576	115	1300	160
5c, d	Isunguata Sermia front	67.1868	50.3418	80	960	260
5e, f	Isunguata Sermia margin	67.1628	50.1617	0	150	330
5g, h	Næsset Kangerlussuaq	67.1545	50.0335	100	390	290
5i, j	Påkitsoq 1/2/3	69.4299	50.2608	120	300	130
–	Inglefield Land	78.0573	67.8978	155	8790	165

Sites are ordered following labelling given in Fig. 1, clockwise from the westernmost Warming Land site. Geographic coordinates are for the translated transect origin (typically near or at the ice margin). Note that the values for Warming Land sites are updated from R02 (N. Henriksen, pers. comm., 2018), and that site names are those given by R02. Translation azimuth is the direction in which the transect was translated horizontally, expressed clockwise from true north. The rightmost three columns are all estimated manually for this study.

Ruth and others (2003) using a laser microparticle detector. This record covers the time span between 60 and 9.5 ka, which is fortuitously contemporaneous with plausible chronostratigraphic interpretations of satellite imagery along part of the northern GrIS margin. While the interactions between dust, algae and seasonal subaerial melting are an area of active research (e.g. Ryan and others, 2018), for the purposes of this study we assume that the marginal surface stratigraphy whose boundaries we mapped can be compared qualitatively to this ice-core dust record from the dry snow zone (e.g. Bøggild and others, 2010).

3. Results

3.1. Satellite imagery at $\delta^{18}O$ transects

Figures 4–6 show both the 2019 S2 mosaic and WV imagery in the vicinity of the available surface $\delta^{18}O$ transects across the GrIS. These comparisons demonstrate that S2 and WV detect fundamentally the same margin stratigraphy. This consistency indicates that the coarser-resolution S2 imagery is sufficient to map key boundaries in surface stratigraphy across the GrIS.

From these subscenes, it is clear that distinct margin surface strata are typically both more coherent and resolvable in northern Greenland, regardless of apparent age and potential sampling bias in the site selection of R02. While such strata have been identified reliably in southern Greenland previously from ground-based sampling and low-altitude aerial mapping (Petrenko and others, 2006; Kurbatov and others, 2010), their surface expression in southern Greenland is ambiguous in the satellite imagery we examined, even in the finer resolution WV imagery. Only at the Påkitsoq site, near where Petrenko and others (2006) sampled, is there a hint of coherent but heavily folded pre-Holocene strata in the WV imagery (Fig. 5j).

When compared against the estimated locations of the $\delta^{18}O$ transects, we find that only the Kronprins Christian Land K/KS sites in northeastern Greenland display a plausible relation between $\delta^{18}O$ and surface stratigraphy at the scale of these subscenes (Figs 4e–h), there, the transects are finely sampled ($\leqslant$5 m), the boundaries between the Holocene, YD and B-A layers are clear, and there is a clear transition in $\delta^{18}O$ values between the LGP and the Holocene. The imprecision of available georeferencing and translation uncertainty prevents a finer-scale assessment of the relation between $\delta^{18}O$ and the layering between the beginning of the B-A and the Holocene. At other sites in northern Greenland, either the coarseness of the $\delta^{18}O$ sampling (Warming Land 1-4, Figs 4a–d), the length of the transect (Warming Land 1-4, Figs 4a–d), the imprecision of the georeferencing (Inglefield Land) or the lack of a clear transition in $\delta^{18}O$ values, perhaps related to periodic surging (Storstrømmen N/NS, Figs 4i, j; Mouginot and others, 2018) prevent additional confirmation of the large-scale chronostratigraphic relation hypothesised by R02. This situation limits us to Kronprins Christian Land K/KS as the type locality for the large-scale $\delta^{18}O$–stratigraphy relation that we seek to exploit (Fig. 2), but we note that this restriction does not impact the interpretation of the previously mentioned finer-scale investigations in southwestern Greenland (e.g. Påkitsoq).

The new Hiawatha Glacier transect we collected is not as finely sampled as that of the R02 Kronprins Christian Land sites and its margin stratigraphy is more complex, with repeated sequences indicating folding (Fig. 6). However, its transitions in $\delta^{18}O$ and δD values match well with satellite-mapped transitions in visual appearance, strongly supporting the $\delta^{18}O$–stratigraphy relation hypothesised by R02. The $\delta^{18}O$ and δD values are not perfectly bimodal between glacial and interglacial periods, but that is expected given the significant variability that is typically present in those values. Further, the best-fit $\delta^{18}O$–δD relation differs significantly between meteoric ice (8.14 ± 0.07; 95% confidence bound) and what we assumed was basal ice prior to sampling (7.85 ± 0.18). Although this difference is small compared to global variability in that relation (e.g. Putman and others, 2019), it is consistent with previous observations of the isotopic differences between meteoric and basal ice (Larsen and others, 2010), further indicating that this layer is not meteoric.

3.2. Margin layer mapping

Our S2 mapping of the bottom of the Holocene, YD and B-A layers, along with the top of the basal ice, generated 242, 144, 145 and 241 discontinuous segments, respectively. These boundaries were mapped as far north as 82.1°N, adjacent to Peary Land in northern Greenland, and as far south as 74.2°N, adjacent to Waltershausen Glacier in eastern Greenland, but the boundary was mostly mapped north of 76.8°N. In terms of well-known major outlet glaciers in northern Greenland, we mostly mapped these boundaries from west of Hiawatha Glacier (northwest) to Storstrømmen (northeast). In terms of ice-drainage systems (Fig. 1), nearly all of the layer segments we mapped were within ice-drainage systems 1.1, 1.2, 1.3, 1.4 and 2.1, with a small portion mapped within system 2.2 (Zwally and others, 2012).

For the bottom of the Holocene layer, the median and maximum segment lengths are 4.2 and 89.5 km, respectively, with a median separation between digitised points of 91 m. The YD,

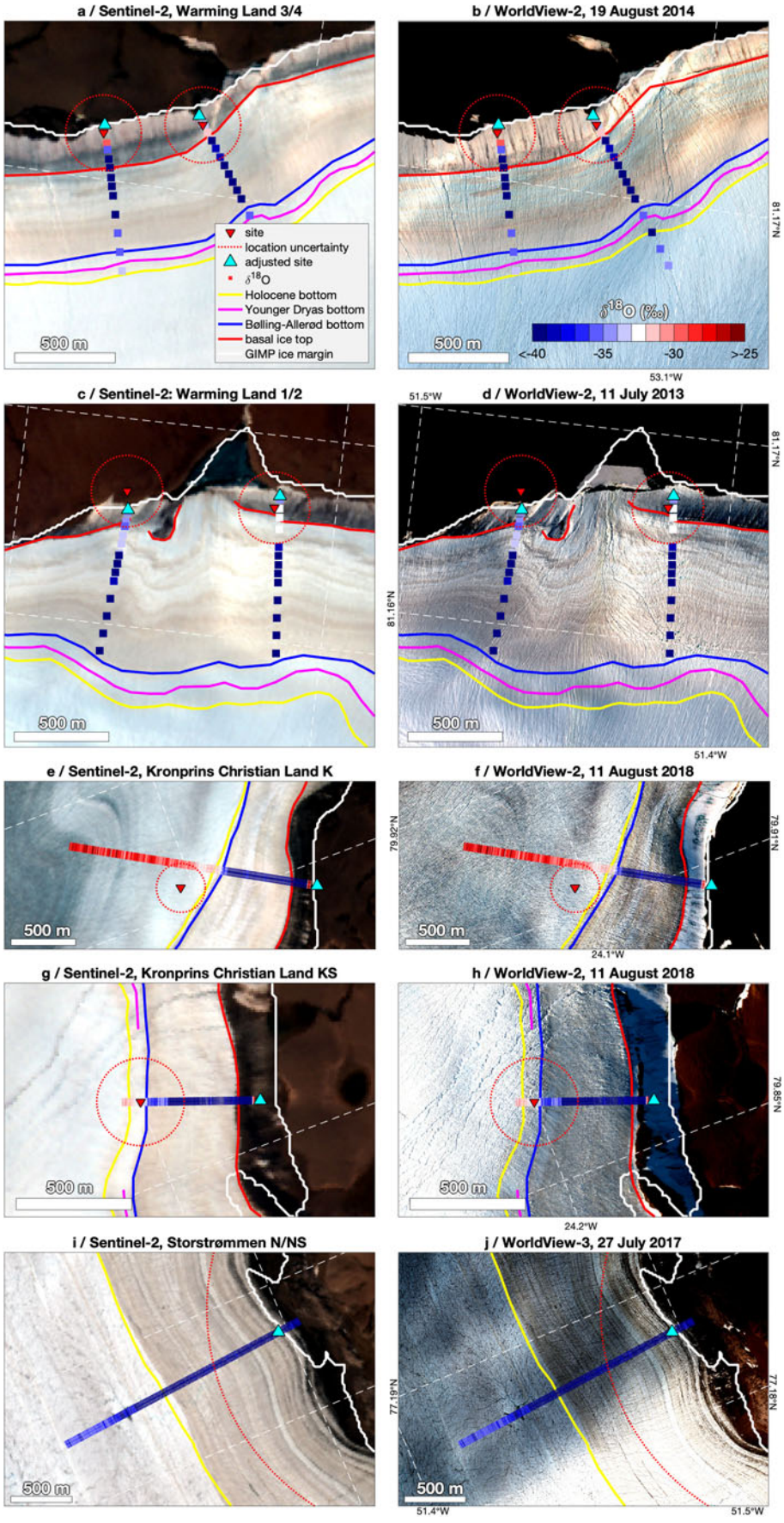

Fig. 4. August 2019 S2 mosaic (left of pair) and WV imagery (right of pair) in the vicinity of available R02 $\delta^{18}O$ surface-sampling sites in northern Greenland (Fig. 1), with $\delta^{18}O$ data overlain at manually corrected position ('adjusted site'), each transect's location uncertainty, and boundaries traced in S2 mosaic only shown for each pair. All image subscenes are contrast-stretched. For panels f and h, brighter snow remains along the margin that obscures the darker basal ice (evident in panels e and g), as was also observed in this region by Bøggild and others (2010). WV sensor and image data are given in the title. Contains Copernicus Sentinel-2 2019 data processed by ESA. WV imagery is copyright 2020 DigitalGlobe Inc.

B-A and basal ice boundaries were less extensively observed and mapped. Their median separation between digitised points was similar (79, 99 and 108 m, respectively), but their median segment lengths were somewhat shorter (1.7, 3.6 and 2.8 km, respectively) and their maximum segment lengths were substantially shorter (26.6, 44.3 and 39.4 km, respectively).

Figure 7 shows two combinations of the horizontal layer thickness between mapped boundaries. In the case of the pre-Holocene

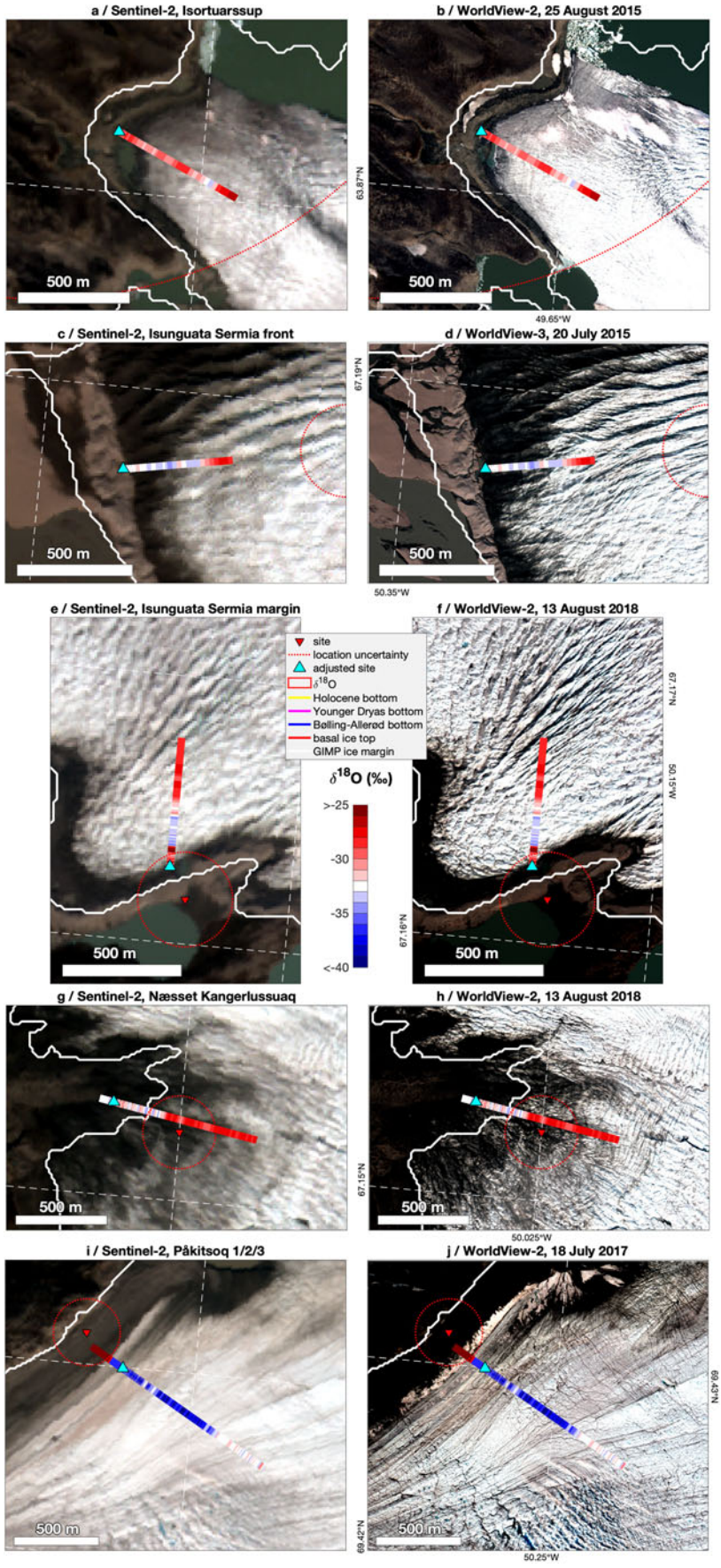

Fig. 5. August 2019 S2 mosaic (left of pair) and WV imagery (right of pair) in the vicinity of available R02 $\delta^{18}O$ surface-sampling sites in southern Greenland (Fig. 1). The format follows Fig. 4. Contains Copernicus Sentinel-2 2019 data processed by ESA. WV imagery is copyright 2020 DigitalGlobe Inc.

meteoric ice thickness, this metric represents an indirect proxy for the potential maximum age of coherent surface stratigraphy originating from periods of general interest. We note that this proxy is complicated by multiple factors, including the surface slope, subsurface boundary dip and the presence of any anomalous margin structures (e.g. plan-view folds). The combined

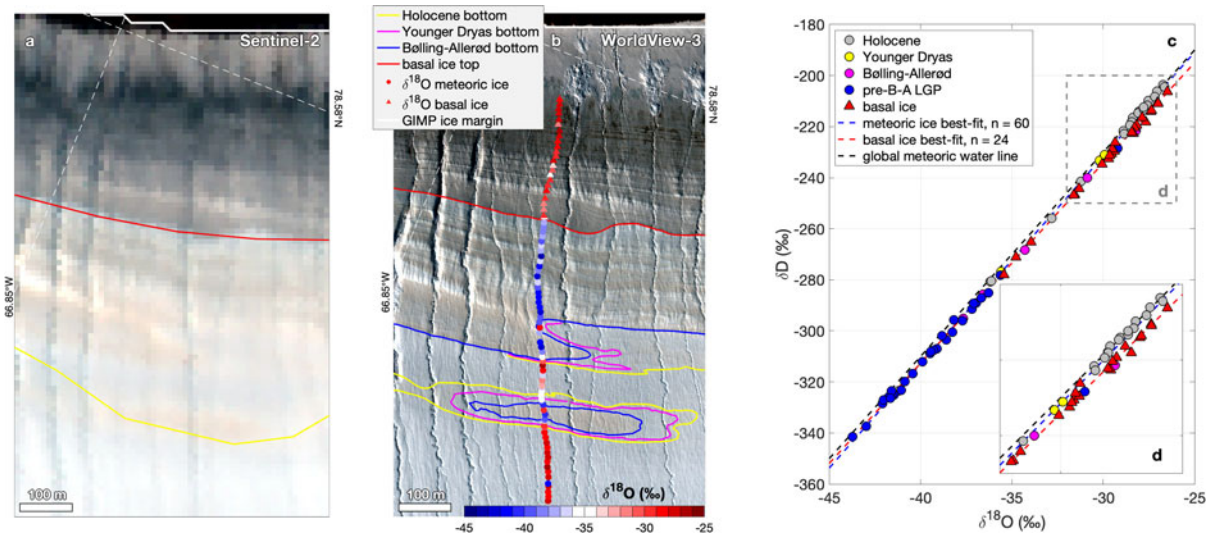

Fig. 6. (a) August 2019 S2 mosaic and (b) 24 August 2018 WV image at the southwestern corner of Hiawatha Glacier, with $\delta^{18}O$ values measured from surface ice samples collected in July 2019 overlain. Image sub-scenes are contrast-stretched. Boundary tracings shown are those mapped using each respective image, i.e. they were traced at substantially different spatial scales. (c) $\delta^{18}O$–δD co-isotope plot with values subdivided by margin region where they were detected. The reference global meteoric waterline is from Craig (1961). (d) Zoom-in of isotopic difference between meteoric and basal ice samples. Contains Copernicus Sentinel-2 2019 data processed by ESA. WV imagery is copyright 2020 DigitalGlobe Inc.

thickness of the YD and B-A layers constitute a fixed period (1.1 + 1.9 = 3.0 kyr) that represents an indirect proxy for the age resolution within that period. While the resolution of the Landsat imagery used to generate the GIMP ice mask is 15 m and that of the S2 imagery is 10 m, we consider these thicknesses to have an uncertainty smaller than or comparable to that of the along-boundary digitisation separation (~100 m). This uncertainty is due to both the precision of our tracing and uncertainty in the delineation of the ice margin, which was traced in imagery nearly two decades older than that which we investigated (Section 2.1).

The median horizontal thickness of pre-Holocene meteoric ice that we mapped is ~714 m (Fig. 7a, Fig. 8). This thickness is typically smaller in northwestern Greenland, as compared to northeastern Greenland. At lower latitudes in northeastern Greenland (<78°N), this thickness sometimes exceeds 2 km. However, these estimates are biased by more complex margin stratigraphy (folding) and the greater presence of nunataks there (e.g. Fig. 12, Appendix A; Section 3.3). Not all nunataks we observe in the S2 mosaic are present in the GIMP ice mask, leading to occasional spuriously high values we could not filter out easily. The thickest (in the margin-perpendicular sense) exposures of pre-Holocene ice occur along the GrIS margin adjacent to northeastern Inglefield Land, southern Daugaard-Jensen Land, southern Warming Land, southeastern Peary Land, southwestern Mylius-Erichsen Land, western Kong Frederik VIII Land, southwestern Kronprins Christian Land and the nunataks of Hertugen af Orléans Land south of Zachariæ Isstrøm (Figs 7a, 8). Elsewhere, such as southwestern Inglefield Land, such exposures can be near-contiguous for tens of kilometres, but their margin-perpendicular length is shorter and harder to interpret.

The median horizontal thicknesses of the YD and B-A layers were not significantly different (81 and 85 m, respectively), and their total median thickness (161 m; Fig. 7b) was less variable across the northern GrIS than the total thickness of pre-Holocene meteoric ice. We attribute this difference in spatial variability to two factors: (1) Their combined median thickness is only ~16 S2 pixels, so it was sometimes difficult to resolve at the fixed map scale we selected for mapping, and thinner exposures of these layers are likely undersampled. (2) This layer pair represents a fixed period of time (3 kyr), whereas the total thickness of pre-Holocene meteoric ice has no fixed period and may vary by tens of thousands of years. At the 10-m resolution of S2, the westernmost extent of detectable, coherent YD and B-A layers is northeastern Inglefield Land (Fig. 8), along the northeastern corner of Hiawatha Glacier; the easternmost extent is near Storstrømmen in Dronning Louise Land.

3.3. Anomalous margin layering

Having mapped the large-scale margin chronostratigraphy of the northern GrIS, we next briefly document anomalous and notable expressions of that stratigraphy (Fig. 9), in particular folded or unusually dark ice.

With one major exception, the map trace of the pre-Holocene stratigraphy in the northwestern half of our study area (i.e. west of 45°W) generally conforms to either the ice margin or the mapped exposure of basal ice (Fig. 12). This exception is the ~35-km stretch of the ice margin immediately west of the southwestern corner of Hiawatha Glacier, Inglefield Land. There, the bottom of the Holocene undulates along-margin at kilometre scales with no discernible relation to the relatively uniform exposure of basal ice. Examination of both the S2 mosaic and finer-resolution WV imagery confirms this pattern and that the bottom of the Holocene ice appears to be repeated perpendicular to the ice margin at a scale of ~200 m (Figs 6, 9a, b). In map view, a portion of the pre-Holocene LGP sequence – but not all of it – is interfingered with Holocene ice. This pattern indicates that the Holocene–LGP boundary is steeply folded there relative to the surface slope, consistent with both the radar-sounding observations of Kjær and others (2018) and the cross-sectional view put forth by Schaefer and others (2009) for a similar pattern within a smaller exposure in southwestern Greenland. The origin of this disturbance is unknown, but any plausible explanation must account for the remarkable horizontal extent of the folding and its apparent synchroneity.

East of ~32°W, plan-view lateral folding of identifiable boundaries occurs intermittently and mostly along the margins of outlet glaciers and nunataks (e.g. Figs 9c, d). This pattern suggests a plunging fold in the layering, i.e. one whose fold axis has a non-

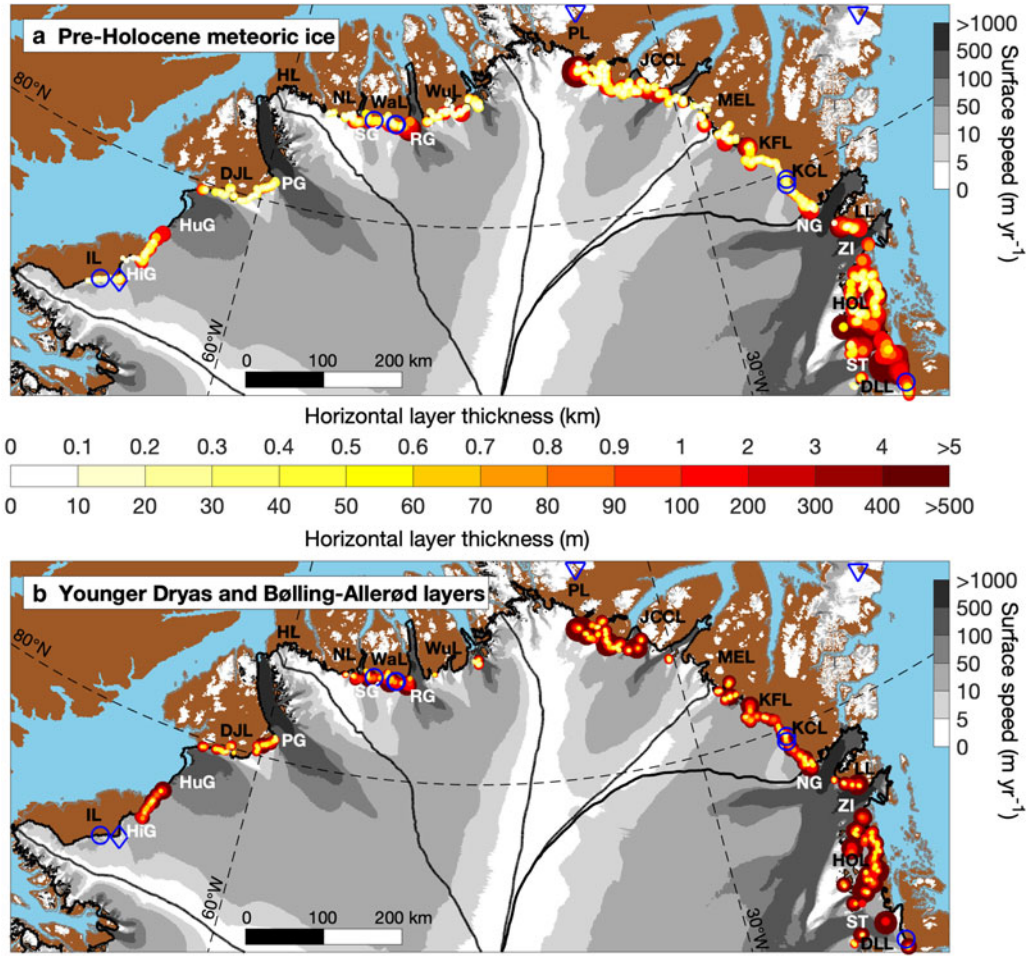

Fig. 7. (a) Horizontal thickness (distance) between the traced bottom of the Holocene layer and either the ice margin, nearby nunataks or the traced top of the basal ice layer, whichever is closest. Background greyscale on ice is surface speed (Joughin and others, 2017), and thick black lines are ice-drainage systems (Zwally and others, 2012). Layer-thickness symbols are scaled by both size and colour, with smaller values shown above larger ones. (b) Same as panel a but the horizontal thickness between the traced bottoms of the Holocene and B-A layers, i.e. the combined horizontal thickness of the YD and B-A layers. Note values assigned to thicknesses differ between panels a and b, per values on top and bottom of colour scale, respectively. Blue symbols denote R02 sites following Fig. 1. Abbreviations in panel a for regions/glaciers: IL: Inglefield Land; HiG: Hiawatha Glacier; HuG: Humboldt Glacier; DJL: Daugaard-Jensen Land; PG: Petermann Glacier; HL: Hall Land; NL: Nyboe Land; SG: Steensby Glacier; WaL: Warming Land; RG: Ryder Glacier; WuL: Wulffs Land; PL: Peary Land; JCCL: J.C. Christensen Land; MEL; Mylius-Erichsen Land; KFL: Kong Frederik VIII Land; KPL: Kronprins Christian Land; NG: Nioghalvfjerdsfjorden Glacier; LL: Lambert Land; ZI: Zachariæ Isstrøm; HOL: Hertugen af Orléans Land; ST: Storstrømmen; DLL: Dronning Louise Land.

negligible dip relative to the near-horizontal ice surface. These folds could arise from past variability in the local ice-flow velocity field, as has been inferred for medial moraines at larger scales on Malaspina Glacier, Alaska (Post, 1972; Hudleston, 2015). However, given that these folds are often seen near nunataks, which indicate locally non-negligible subglacial roughness, we consider it more likely that they are due to significant lateral shear as ice flows approximately these obstacles.

In the part of northeastern Greenland, north of Nioghalvfjerdsfjorden Glacier, we observe the extent of an unusually dark exposure of ice that clearly originated during the Holocene epoch and was previously identified by Bøggild and others (1996) (Fig. 9e). This dark ice is typically found within a layer that lies between ~2 and 5 km inland of the traced bottom of the Holocene and is adjacent to Kronprins Christian Land, where the type locality for the chronostratigraphic relation was first identified by R02 (Fig. 2). While we cannot yet assign a specific age range to this layer, its expression qualitatively resembles that of the better-known dark layer in southwestern Greenland (Fig. 9f), which also appears to be partly related to Holocene dust present in the ice (Bøggild and others, 1996; Wientjes and others, 2012; Ryan and others, 2018).

3.4. Potential oldest surface-exposed ice in Greenland

A question that naturally arises from our mapping is: where is the oldest ice? Our coarse mapping of chronostratigraphy of the northern GrIS margin reveals two distinct sites with extensive and coherent pre-Holocene stratigraphy that are ~38 km apart and adjacent to Warming Land (Fig. 10; Figs 13 and 14, Appendix A). Warming Land is the mostly deglaciated region bounded by Steensby Glacier to the west and Ryder Glacier to the east, both of which are major marine-terminating outlet glaciers in northern Greenland (Fig. 7a). At both sites, more than 20 >10-m-wide layers below the B-A are distinguishable and mostly conformable with each other. We distinguish these layers by their alternating pattern of colour and brightness, and they are typically detectable for several kilometres along-margin. For pre-B-A LGP layers at these two sites, there is no indication of plan-view folding, as observed elsewhere in northern Greenland (e.g. Figs 9c, d). This pattern suggests that layering at these sites is not repeated due to folding, but instead represents a contiguous period of ice deposition and subsequent flow.

Because we hypothesise that the layers' colour and brightness is primarily due to variable englacial dust concentration, following Bøggild and others (2010), we compared the Warming Land sites'

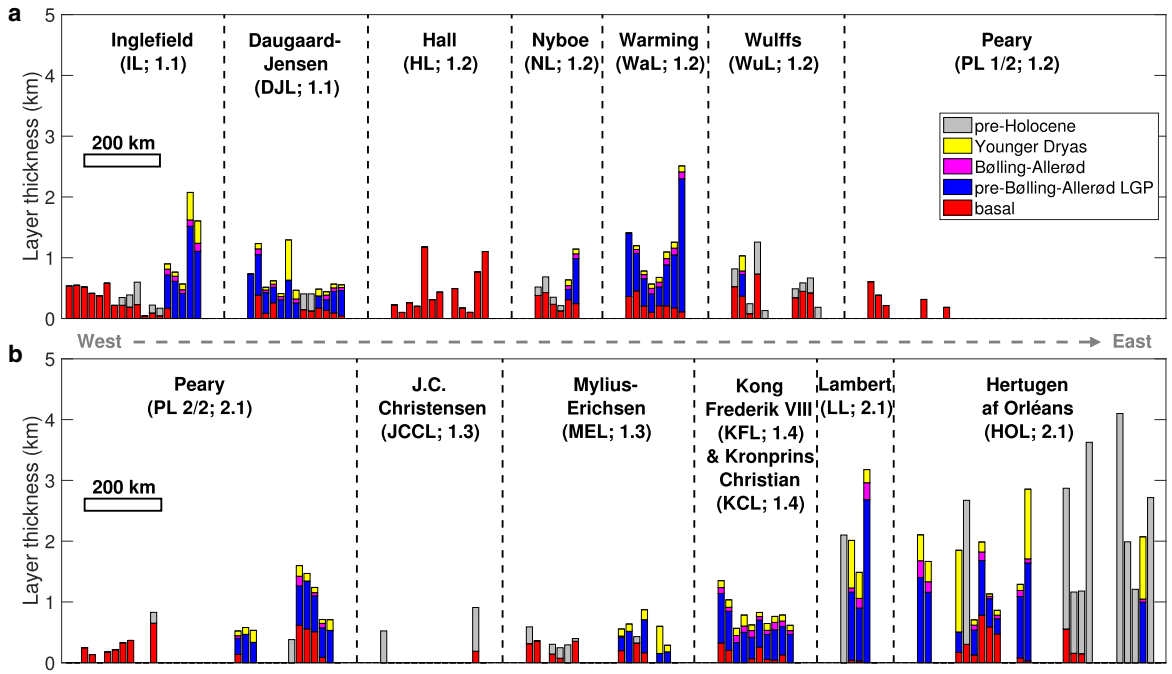

Fig. 8. Binned median horizontal thickness of each mapped layer (distance between either two traced boundaries or one traced boundary and ice margin), separated regionally by margin-adjacent land (vertical dashed lines) Abbreviations follow Fig. 7, and the number afterward is the GrIS drainage basin following Fig. 1. Along-margin bin length is 20 km. The horizontal scale bar panel is valid only within each land, i.e. it is not continuous between lands and there is an artificial 100-km buffer between each land's mapped exposures. Where the bottom (beginning) of the Holocene was mapped, but no other conformal boundaries below (older) than that, the layer is classified as 'pre-Holocene'. (a) The western half of our study area, including the western half of Peary Land ('PL (1/2)'). (b) The eastern half of our study area, beginning with the eastern half of Peary Land ('PL (2/2)'). Note that these thickness distributions filter out nunatak-adjacent traced boundaries as best as possible, so Dronning Louise Land is not shown.

layering to the nearest available multi-millennial ice-core record of dust concentration, which is from the NorthGRIP ice core located more than 700 km southeast of these two sites (Figs 10e, f). We briefly explored the mathematical relation between NorthGRIP dust concentration and WV-observed colour but could not establish a simple relation, so this possibility is left to future investigations. Nevertheless, a qualitative but surprisingly good visual relation is apparent between the two sites' layering and the NorthGRIP dust record. Alternating browner and bluer layers exposed near Warming Land appear to be sequenced consistently with dustier and cleaner periods, respectively, in the NorthGRIP ice core. Further, the longer the dusty period in the NorthGRIP record, the wider the exposed dusty layer at Warming Land, with the same relation holding generally for less dusty periods and cleaner layers. We, therefore, hypothesise that the age of LGP ice exposed at these two sites extends back in time to a period well before to the Bølling–Allerød interval (i.e. older than 14.7 ka) – perhaps to before ~55 ka – and that multiple Dansgaard–Oeschger events are recorded there. While this apparent relation sets aside the potential complexity inherent to tens of millennia of ice flow between deposition in the ice-sheet interior and present-day emergence at the margin, this hypothesis can simply explain the remarkable correspondence between these independent records.

While R02 hypothesised the presence of surface-exposed ice from the Last Interglacial Period (Eemian; ~130–115 ka) elsewhere on the GrIS margin, that inference could not be confirmed by $\delta^{18}O$ measurements alone. Hence, we suggest that the Warming Land sites discussed above represent the oldest coherent exposures of late-Pleistocene ice in the northern hemisphere identified so far. In Antarctica, yet older surface-exposed ice has been found in blue ice regions and the Dry Valleys (e.g. Schäfer and others, 2000; Sinisalo and Moore, 2010; Buizert and others, 2014; Yan and others, 2019).

3.5. Basal ice properties

During our satellite mapping of margin layering, we made four main observations of the basal ice layer that warrant reporting here. While we examined the northern GrIS margin at fine spatial scales, we also conducted a larger-scale examination of the whole of the GrIS margin. We found that the basal ice exposures detectable in the S2 mosaic were much more common in northern Greenland (our study area) than elsewhere. So, while we do not consider our mapping of the top of the basal ice to be comprehensive for the whole of Greenland, we consider it sufficient to support the following observations.

The first observation is that – when examined in finer-resolution WV imagery – the basal ice layer is itself laminated at multi-meter scales, as also reported by R02 but now visible at larger scales (e.g. Fig. 9b). This pattern is typically margin-parallel and suggests that the basal ice layer was formed episodically. It is not immediately clear if this pattern is consistent with the laminated basal ice facies that are sometimes observed in situ (e.g. Knight, 1997). During our sampling at Hiawatha Glacier (Fig. 6), we also observed sub-meter laminations in the basal ice. Where supraglacial streams incised into the basal ice, these laminations were steeply dipping (subvertical).

The second observation is that – for any given traced segment of the top of the basal ice – this boundary appears to be approximately isochronal, as indicated by where/when it meets the Holocene or LGP ice above it (Fig. 12). This observation suggests that the apparent unconformity at this boundary is due to either an accumulation hiatus, ice erosion or basal freeze-on that occurred at approximately the same time. Further, the age at which this unconformity meets overlying younger ice appears to increase as one moves farther east and north across northern Greenland (Fig. 12). Adjacent to southwestern Inglefield Land, the top of the basal ice appears to intersect early Holocene ice, whereas adjacent to Warming Land or Kronprins Christian

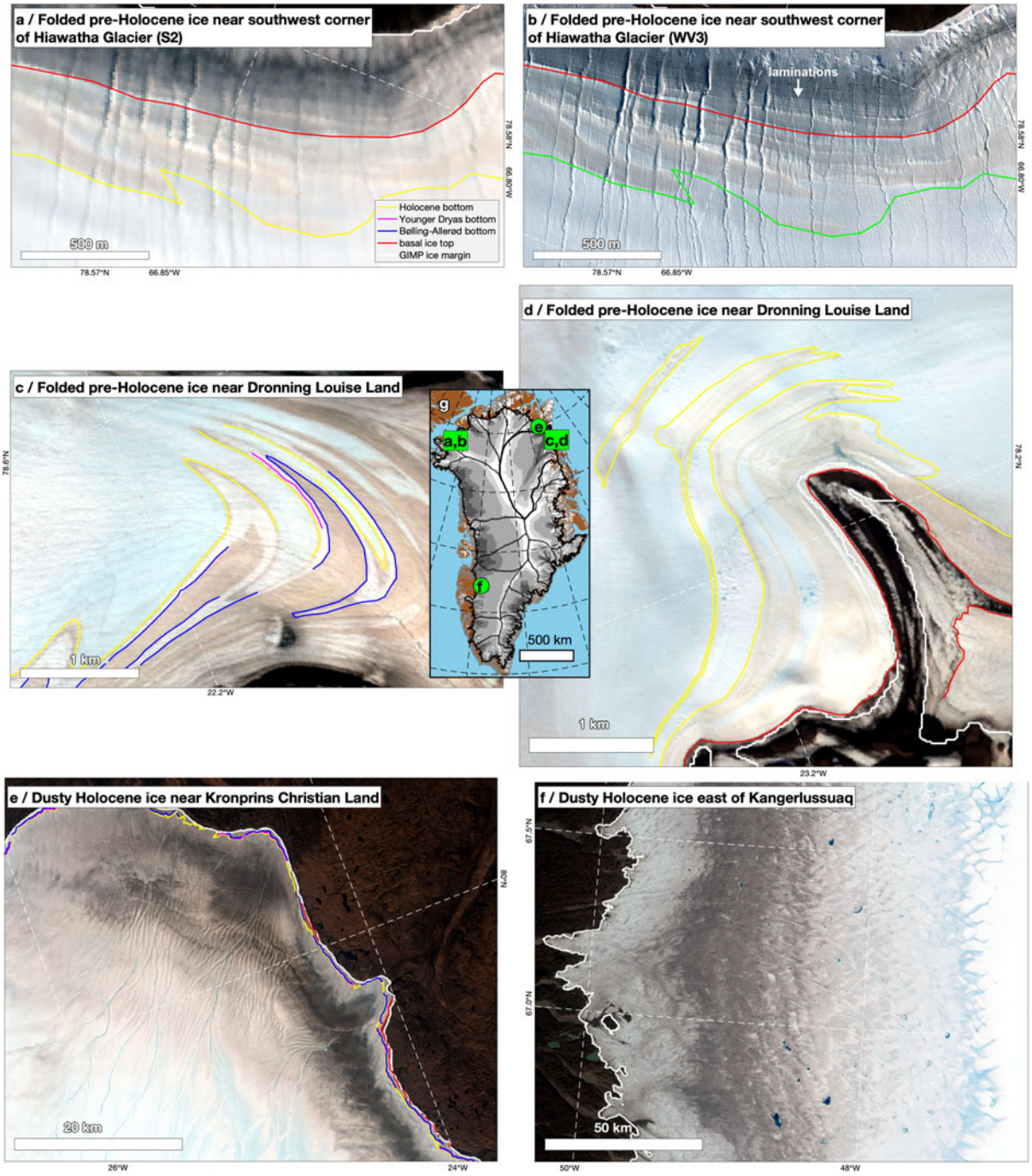

Fig. 9. Subscenes of contrast-stretched August 2019 S2 mosaic (except panel b, which is WV) showing example anomalous margin structures and layering across Greenland. (a) The ice-sheet margin southwest of Hiawatha Glacier in northwestern Greenland showing regular folding of pre-Holocene ice. (b) Same as panel a but using WV imagery. (c) and (d) Apparent plunging folds in emerging stratigraphy at the ice-sheet margin near Dronning Louise Land in northeastern Greenland. (e) The ice-sheet is bordering Kronprins Christian Land in northeastern Greenland and (f) east of Kangerlussuaq in southwestern Greenland, showing similar gray high-dustiness regions within Holocene ice. (g) Map of Greenland showing the location of subscenes, where grayscale is surface speed, as shown in Fig. 7. Contains Copernicus Sentinel-2 2019 data processed by ESA. WV imagery is copyright 2020 DigitalGlobe Inc.

Land, that intersection appears to occur sometime during the pre-B-A LGP.

The third observation is that we mapped basal ice mostly adjacent to local highlands in the bed topography of northern Greenland (Fig. 11a). This observation is unsurprising, because we did not expect to be able to map surface-exposed layering extensively within or alongside most of the heavily sheared, major outlet glaciers that flow through subglacial troughs. However, it could be the most significant of the four, as it establishes a relatively simple spatial relation between the presence of surface-exposed basal ice and higher bed topography. The northern shear margin of Humboldt Glacier (southern Daugaard-Jensen Land) is perhaps the clearest deviation from that pattern, where basal ice is observed immediately adjacent to the subglacial trough that Humboldt Glacier flows through.

Finally, we note that basal ice is observed at the margin of ice-drainage systems that can be either predominantly frozen or thawed (Fig. 11b). Somewhat more basal ice appears present adjacent to predominantly frozen ice-drainage systems in far northern Greenland, but the margin abutting Daugaard-Jensen Land and Kronprins Christian Land is downstream of ice whose bed is likely thawed. Given the preservation of basal ice at these locations, this observation could reflect a limitation of the present basal thermal state synthesis (e.g. Chu and others, 2018). This observation also

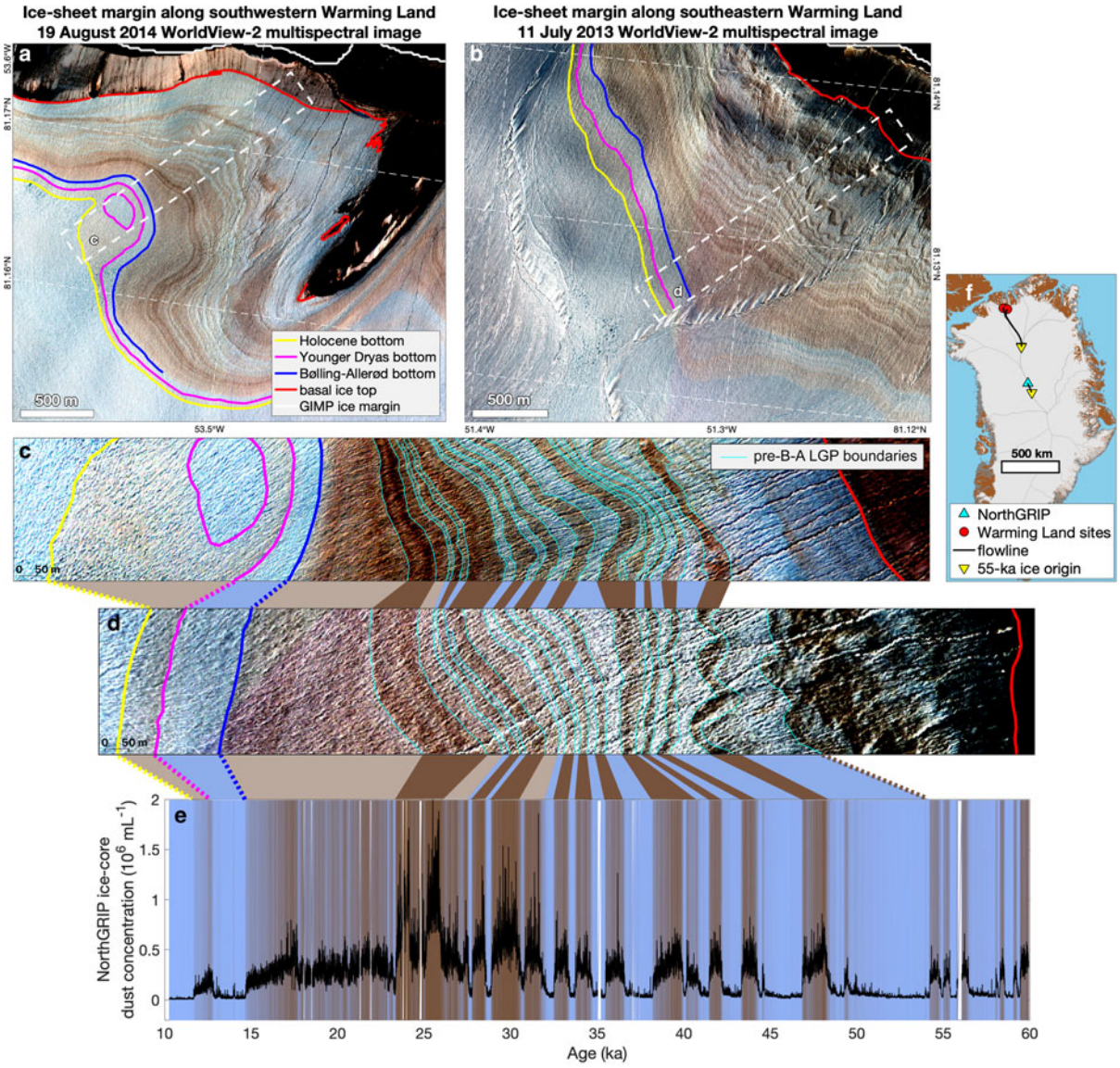

Fig. 10. Contrast-stretched WV multispectral imagery of the GrIS margin adjacent to (a, c) southwestern and (b, d) southeastern Warming Land, in northern Greenland between Steensby and Ryder glaciers. Boxes between panels c and d identify potential matches in periods of higher apparent dust concentration between the two sites and (e) the dust concentration measured in the NorthGRIP ice core (Ruth and others, 2003). In panel e, the background color is scaled between blue (low dust concentration) and brown (high dust concentration) to illustrate potential matches. (f) Map of Greenland showing the location of relevant sites and estimated upstream origin of 55-ka ice, calculated using a Greenland-wide surface-velocity field (Joughin and others, 2017) and a shape factor of 0.8. WV imagery is copyright 2020 DigitalGlobe Inc.

suggests that cold-based mechanisms likely contribute to the formation of the basal ice outcrops we mapped (Knight, 1997). Very few of the basal ice 'plumes' identified by Leysinger Vieli and others (2018) – which they hypothesise are formed by basal freeze-on – are located beneath the ice that is presently flowing toward land-terminating margins (Fig. 11b). The radar-inferred distribution of Eemian ice is more widespread than the basal plumes (Fig. 11b), but it is difficult to constrain how thick such ice would be if any of it does indeed emerge at the margin.

4. Discussion

4.1. Implications for in situ margin sampling

A surprising outcome of our study is that – despite its successful subsequent application by later efforts – the visual pattern identified by R02 is only well supported by our comparison of satellite imagery and $\delta^{18}O$ transects at a pair of adjacent sites in northeastern Greenland (Kronprins Christian Land K/KS, Figs 3, 4e–h) and our Hiawatha Glacier site (Fig. 6). We find that the sites sampled by R02 constitute a good diversity of expressions of margin layering, but for various reasons, the majority of them were suboptimal relative to their stated goal of producing 'important and (cheap) supplements to ice core records', particularly for the northern GrIS. This discovery does not invalidate in situ age interpretations at other sites, which often have more complex margin layering, because more detailed sampling commensurate to that layering complexity was performed, along with additional chemical analyses. However, this outcome does warrant additional surface sampling to refine the visual interpretation we applied across the northern GrIS.

Two previously unexplored sites of note are those that we identified along the ice margin adjacent to Warming Land, where surface-exposed strata are exceptionally well preserved and likely extend well into the LGP (Fig. 10). These identifications highlight the value of satellite remote sensing for site reconnaissance of ice-margin stratigraphy, because although these two promising sites are 38 km apart, they are both <6 km from

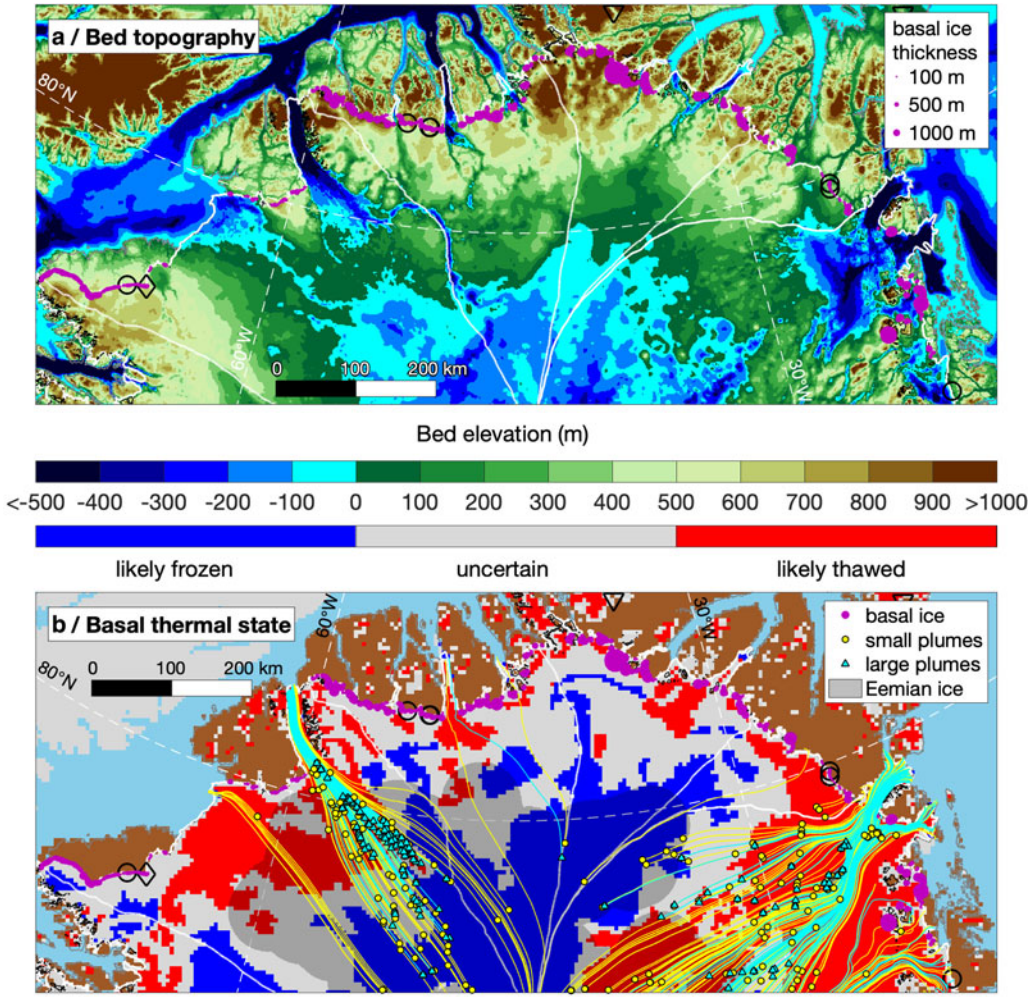

Fig. 11. The extent of basal ice layer superimposed on (a) BedMachine v3 bed topography (150-m grid; Morlighem and others, 2017) and (b) the likely basal thermal state (5-km grid; MacGregor and others, 2016*b*). Marker size for basal ice is scaled by its margin-perpendicular horizontal extent (thickness). For panel b, both mapped inland basal ice 'plumes' (Leysinger-Vieli and others, 2018) and radiostratigraphy-inferred extent of the top of Eemian ice (115-ka isochrone) in the GrIS interior are overlain (MacGregor and others, 2015); streamlines (solid lines) for basal units calculated using surface-velocity field (Joughin and others, 2017).

opportunistic $\delta^{18}O$ transects collected in 1985 (Table 1; Figs 4a–d). However, both sites are logistically challenging to reach, as they are more than 500 km from the nearest permanent settlement in Greenland and more than 200 km from Alert, Canada. This situation exemplifies the present balance of risk and reward for accessing surface-exposed paleoclimatically distinct ice in Greenland, i.e. the most promising sites are located in some of the most remote regions of the island.

The identification of additional promising sites for margin ice sampling in Greenland is also important for novel measurements of ice properties. While modern measurements of water isotopes and major ion concentrations require only a few millilitres of meltwater (e.g. Bailey and others, 2019), measurements of isotopic or mass concentrations of less common impurities in ice can either require or benefit from significantly larger samples (in some cases >100 kg) that far exceed those of typical ice cores or reasonable allocations thereof (e.g. Steig and others, 1998; Petrenko and others, 2009; Petaev and others, 2013; Buizert and others, 2014; Koll and others, 2019). Wide surface exposures of apparently well-behaved layers in the northern GrIS offer the potential for effectively unlimited access to coherent Holocene and pre-Holocene ice at higher temporal resolution than has been possible for some methods that require bulk ice sampling. The northerly reach of these sites suggests they may also represent better proxies for past sea ice extent in the Arctic Ocean than existing deep Greenland ice cores, because surface-exposed ice there likely originates from farther north than those cores (Fig. 10f). However, recent work suggests that ice originating from the GrIS interior is unlikely to be as valuable as that from more coastal Arctic ice caps in constraining past sea ice extent (Rhodes and others, 2018).

4.2. Broader applications of mapping margin layering

The surface-exposed boundaries that we mapped constitute isochrones (or an unconformity, in the case of the top of the basal ice) that are direct visual analogues to those interfaces regularly mapped by radar sounding in the interior of the ice sheet. Shallow radar sounding of Antarctic blue ice areas has demonstrated correlations between mapped reflections and surface-isotopic profiles (e.g. Winter and others, 2016). However, it is often difficult to trace deep radiostratigraphy within ~100 km of the GrIS margin with the most widely deployed radar sounders (MacGregor and others, 2015; Florentine and others, 2018), and we did not observe coherent surface stratigraphy in our S2 mosaic more than ~100 km inland of the margin because of persistent firn cover in the accumulation zone. Separately, we examined dozens of radargrams intersecting the northern margin that were collected in 2011 and 2014 by Operation IceBridge, and we found that they consistently failed to detect coherent radiostratigraphy there. Thus, the convergence of coherent surface- and radar-mapped layers is rare,

but it has been demonstrated at Hiawatha Glacier by Kjær and others (2018) using the latest radar-sounder technology.

Just as ice-sheet-wide maps of radiostratigraphy could be used to constrain and initialise ice-flow models (e.g. Clarke and others, 2005; MacGregor and others, 2016*a*; Born, 2017; Goelzer and others, 2018), the surface layers mapped in this study could serve a similar purpose for models that can leverage this information. We are not aware of any large-scale model of the GrIS that is presently equipped to ingest these data directly, although Gilbert and others (2016) did find that a thermomechanical ice-flow model of the Barnes Ice Cap based on Elmer/Ice could successfully reproduce both the borehole-observed depth and the apparent rheological contrast of the Pleistocene–Holocene transition. We recognise that assimilation of these surface strata is unlikely to precede assimilation of radiostratigraphy for several reasons: (1) Observations of the former are not as widespread; (2) The horizontal separation of these boundaries is often significantly less than the spatial resolution of present-generation ice-sheet models; (3) Several additional processes complicate modelling of margin layering, as compared to radiostratigraphy in the accumulation zone (e.g. margin migration, surface melting, seasonally transient supraglacial and subglacial hydrology, formation and advection of basal ice).

While this study is the first to map pre-Holocene margin layering across a substantial portion of the GrIS margin, it has several limitations that could be improved upon in future efforts. Foremost is the clear improvement in boundary identification when using finer-resolution WV imagery. The five-to-eight-fold improvement in spatial resolution with only a single bit loss in radiometric resolution (as compared to S2) substantially improves the quality of our pre-Holocene boundary mapping (e.g. Fig. 10). However, the greater data volume of WV imagery and its reduced availability in northern Greenland during our period of interest (late summer) limited the utility thereof to specific narrow regions of interest (Figs 4, 9, 10). A second limitation is the use of manual boundary tracing, whose trade-offs were discussed in Section 2.2. A more substantial effort to investigate robust automated identification of surface-exposed layers could result in a more reliable and widespread mapping of GrIS margin stratigraphy, for both Holocene and pre-Holocene layers. Finally, we reiterate that additional in situ surface measurements of $\delta^{18}O$ values and comparison with dated deep ice cores would improve confidence in the boundary ages that we have assumed in this study.

Our results also evince a potential terrestrial analogue to remote-sensing studies of ice masses elsewhere in the Solar System, in particular the northern polar layered deposits (NPLD) on Mars. There, numerous layers of variable dustiness are also observed by both satellite-based imaging and radar sounding (e.g. Christian and others, 2013; Lalich and others, 2019). These layers outcrop along the margins of the NPLD and have been linked statistically to nearby radiostratigraphy, but no in situ samplings has yet been performed, despite its potential value in deciphering recent Martian climate history. The northern GrIS is remote – but less so than Mars – and the warmer, faster GrIS is an imperfect analogue to the colder, near-static NPLD. However, future exploration of the margin of the northern GrIS could better constrain the geometric and englacial conditions that result in detectable surface and englacial stratigraphy. Such data could inform instrument requirements for future interplanetary missions to study the Martian climate history recorded by the NPLD (Smith and others, 2020*b*).

4.3. The significance of northern Greenland's basal ice

An outstanding question raised by our examination of the northern margin of the GrIS is the significance of the widespread basal ice whose upper boundary we mapped (Fig. 11). Margin-exposed basal ice is famously complex, and our remote observations and limited in situ sampling cannot substitute for more detailed direct investigation thereof, so we cannot yet reliably interpret its apparent composition or formation mechanism from space (e.g. Knight, 1997; Larsen and others, 2010). While our in situ measurements indicate that unit is indeed basal ice (Fig. 6), it is not yet certain that the unit we mapped can strictly be considered basal ice, as it is not consistently sediment-rich, nor have we demonstrated that all this ice has flowed within meters of the bed. Regardless, in the basal ice taxonomy put forth by Knight (1997), the most plausible interpretation is that we have mapped the top of dispersed facies, i.e. 'ice that has been so affected by metamorphic processes close to the bed that it displays the features of neither meteoric glacier ice nor basally frozen ice.' Such ice is expected to have a lower debris content than the dark brown ice-cemented debris layers sometimes observed at the base of Greenlandic glaciers (e.g. Larsen and others, 2010). This interpretation is consistent with the widespread geographic distribution of the unit (Fig. 11), but not with the occasional observations of distinct strata apparent in WV imagery (Figs 9a, b, 10; Figs 13, 14). However, Knight (1997) acknowledges that a continuum of basal ice facies is sometimes observed, and that stratified basal ice is more commonly observed below dispersed facies, which is roughly consistent with our observations and others in Greenland (e.g. Larsen and others, 2010).

Basal ice formation is generally attributed to cold-based glacier flow. While our basal ice distribution is somewhat consistent with being the downstream product of cold-based ice flow, it is not conclusively so, and the basal thermal state could easily have varied in the past (Fig. 11b). However, geologic observations of the deglaciated forelands across much of northern Greenland also suggest long periods of minimally erosive, cold-based glacier conditions, even during glacial periods with a greater ice extent (e.g. Pedersen and others, 2019). A simple synthesis of those observations and ours could be that – outside of the tributary regions for major outlet glaciers and other anomalous subglacial structures – a frozen basal thermal state has persisted beneath the northern GrIS during most of the LGP and the Holocene. Otherwise, widespread pre-Holocene and basal ice are less likely to have survived and the deglaciated landscape would indicate greater long-term erosion rates. Absent additional direct observations of the ice unit whose top we mapped, the above arguments are speculative, but they can plausibly explain several of our observations and warrant further consideration – potentially as targets for studies of the past flow of the GrIS.

5. Conclusions

We synthesised existing observations of surface stratigraphy along the margin of the GrIS with a new satellite-based mapping of key boundaries in that stratigraphy along its northern margin. Effectively, we leveraged a decades-old insight from field observations into the first large-scale evaluation of the age of the northern margin of the GrIS. We described both typical and anomalous margin exposures across northern Greenland and identified promising sites for future recovery of paleoclimatically valuable ice, of which two sites adjacent to Warming Land hold the most promise. We find that large exposures of basal ice are more common across the margin of the northern GrIS than previously known, but that the significance of these exposures remains unclear. We speculate that they indicate the long-term persistence of cold-based conditions beneath most of the northern GrIS.

This study was enabled by access to large volumes of satellite imagery that could be processed efficiently and remotely into a mosaic of direct scientific value. Our approach favoured

simplicity, speed and reliability in the mosaic generation and boundary tracing over methodological sophistication, and as a result, we were able to explore a large portion of the GrIS efficiently. We suggest that future remote-sensing studies of the GrIS and other ice masses considering similarly large scales use these resources to accelerate studies of difficult-to-access regions.

Supplementary material. The supplementary material for this paper can be found at https://doi.org/10.1017/jog.2020.62 The JavaScript code used to generate the filtered August 2019 S2 mosaic within Google Earth Engine is provided in Supplementary File 1 as a plain text file. The layer boundaries we traced are available as ESRI shapefiles in Supplementary File 2 as a zipped archive, for which the projection used is EPSG:3413 (NSIDC Sea Ice Polar Stereographic North). Supplementary Files 3–5 are video animations whose snapshots are shown in Figs 12–14, respectively (Appendix A), and have a standard 1080p resolution in MPEG-4 format. The frame rate of Supplementary File 3 is 2 fps for easy pausing between scenes and boundary overlays, whereas, for Supplementary Files 4, 5, it is 30 fps.

Data. Some of the satellite data presented in this paper are freely available and archived online. In particular, the S2 mosaic is presently available as a cloud-served basemap within the ITS_LIVE QGIS project file for Greenland (Gardner and others, 2020). The source URL for that mosaic can be added as a raster layer within any QGIS project. The MATLAB script used to process the data used in this study and to generate the figures is freely available from the corresponding author (JAM) upon request.

Acknowledgements. We thank the Goddard Fellows Innovation Challenge for supporting JAM's fieldwork and data analysis. We thank ESA/Copernicus for unrestricted access to the S2 imagery used in this study and Google Earth Engine for free access to their cloud computing resources. We thank the Polar Geospatial Center (PGC) and DigitalGlobe Inc. for access to WV imagery, and the PGC for ArcticDEM. We recognise the pioneering efforts of the late Niels Reeh, whose work provided both the inspiration and basis for this study. We thank Hans Oerter for providing a digital copy of $\delta^{18}O$ data collected several decades ago and permission to use his photograph, and Niels 'Oscar' Henriksen for improved coordinates of the four Warming Land sites and valuable discussions concerning sampling methods there. We thank Pierre Beck, Anders Bjørk, Ludovic Brucker, Jessy Jenkins, Hans-Peter Marshall, Jérémie Mouginot and Lincoln Pitcher for equipment loans and fieldwork assistance, and John Sonntag for permission to use his photograph. Finally, we thank Chief Editor Hester Jiskoot, Scientific Editor Beatá Csathó and two anonymous reviewers for their constructive reviews of the manuscript.

Author contributions. All authors contributed to both the data interpretation and writing. JAM conceived the study and led the fieldwork, data analysis, interpretation and writing. MAF led the mosaic generation, WTC led the data archaeology, NKL and KKK led the interpretation of the basal ice mapping, and JMW led the laboratory analysis.

References

Aciego SM, Cuffey KM, Kavanaugh JL, Morse DL and Severinghaus JP (2007) Pleistocene ice and paleo-strain rates at Taylor Glacier, Antarctica. *Quaternary Research* **68**(3), 303–313. doi: 10.106/j.yqres.2007.07.013.

Bailey H, Klein ES and Welker JM (2019) Synoptic and mesoscale mechanisms drive winter precipitation $\delta^{18}O/\delta^{2}H$ in south-central Alaska. *Journal of Geophysical Research Atmospheres* **124**, 4252–4266. doi: 10.1029/2018JD030050.

Bøggild CE, Brandt RE, Brown KJ and Warren SG (2010) The ablation zone in northeast Greenland: ice types, albedos and impurities. *Journal of Glaciology* **56**(195), 101–113. doi: 10.3189/002214310791190776.

Bøggild CE, Oerter H and Tukiainen T (1996) Increased ablation of Wisconsin ice in eastern North Greenland: observations and modelling. *Annals of Glaciology* **23**, 144–148. doi: 10.3189/S0260305500013367.

Born A (2017) Tracer transport in an isochronal ice-sheet model. *Journal of Glaciology* **63**(237), 22–38. doi: 10.1017/jog.2016.111.

Buizert C and 10 others (2014) Radiometric ^{81}Kr dating identifies 120,000-year-old ice at Taylor Glacier, Antarctica. *Proceedings of the National Academy of Sciences* **111**(19), 6876–6881. doi:10.1073/pnas.1320329111.

Christian S, Holt JW, Byrne S and Fishbaugh KE (2013) Integrating radar stratigraphy with high resolution visible stratigraphy of the north polar layered deposits, Mars. *Icarus* **226**(2), 1241–1251. doi: 10.1016/j.icarus.2013.07.003.

Chu W, Schroeder DM, Seroussi H, Creyts TT and Bell RE (2018) Complex basal thermal transition near the onset of Petermann Glacier, Greenland. *Journal of Geophysical Research Earth Surface* **123**, 985–995. doi: 10.1029/2017JF004561.

Clarke GKC, Lhomme N and Marshall SJ (2005) Tracer transport in the Greenland ice sheet: three-dimensional isotopic stratigraphy. *Quaternary Science Reviews* **24**(1–2), 155–171. doi: 10.1016/j.quascirev.2004.08.021.

Craig H (1961) Isotopic variations in meteoric waters. *Science (New York, N.Y.)* **133**(346), 1702–1703.

Fahnestock MA and 5 others (2016) Rapid large-area mapping of ice flow using Landsat 8. *Remote Sensing of the Environment* **185**(C), 84–94. doi: 10.1016/j.rse.2015.11.023.

Fahnestock MA, Bindschadler RA, Kwok R and Jezek KC (1993) Greenland Ice Sheet surface properties and ice dynamics from ERS-1 SAR imagery. *Science (New York, N.Y.)* **262**, 1530–1534.

Florentine C, Harper JT, Johnson JV and Meierbachtol T (2018) Radiostratigraphy reflects the present-day, internal ice flow field in the ablation zone of western Greenland. *Frontiers in Earth Science* **6**, 1728–1711. doi: doi:10.3389/feart.2018.00044.

Gardner AS, Fahnestock MA and Scambos TA (2020) ITS_LIVE Regional Glacier and Ice Sheet Surface Velocities. Data archived at National Snow and Ice Data Center. doi:10.5067/6II6VW8LLWJ7.

Gilbert A and 6 others (2016) Sensitivity of Barnes Ice Cap, Baffin Island, Canada, to climate state and internal dynamics. *Journal of Geophysical Research Earth Surface* **121**, 1516–1539. doi: 10.1002/2016JF003839.

Goelzer H and 30 others (2018) Design and results of the ice sheet model initialisation initMIP-Greenland: an ISMIP6 intercomparison. *The Cryosphere* **12**(4), 1433–1460. doi: 10.5194/tc-12-1433-2018.

Gorelick N and 5 others (2017) Google Earth Engine: planetary-scale geospatial analysis for everyone. *Remote Sensing of the Environment* **202**, 18–27. doi: 10.1016/j.rse.2017.06.031.

Hooke RL (1976) Pleistocene ice at the base of the Barnes Ice Cap, Baffin Island, N.W.T., Canada. *Journal of Glaciology* **17**(75), 49–59. doi: 10.3189/S0022143000030719.

Hooke R LeB (2020) Chapter 14: Finite strain and the origin of foliation. In *Principles of Glacier Mechanics*, 3rd Edition. United Kingdom: Cambridge University Press, 387–407.

Howat I (2017) MEaSUREs Greenland Ice Mapping Project (GIMP) Land Ice and Ocean Classification Mask, Version 1, NASA National Snow and Ice Data Center Distributed Active Archive Center. doi:10.5067/B8X58MQBFUPA.

Howat IM, Negrete A and Smith BE (2014) The Greenland Ice Mapping Project (GIMP) land classification and surface elevation data sets. *The Cryosphere* **8**(4), 1509–1518. doi: 10.5194/tc-8-1509-2014.

Hudleston PJ (2015) Structures and fabrics in glacial ice: a review. *Journal of Structural Geology* **81**(C), 1–27. doi: 10.1016/j.jsg.2015.09.003.

Joughin IR, Smith BE and Howat IM (2017) A complete map of Greenland ice velocity derived from satellite data collected over 20 years. *Journal of Glaciology* **64**(243), 1–11. doi: 10.1017/jog.2017.73.

Kjeldsen KK and 15 others (2015), Spatial and temporal distribution of mass loss from the Greenland Ice Sheet since AD 1900. *Nature* **528**(7582), 396–400, doi:10.1038/nature16183.

Kjær KH and 21 others (2018) A large impact crater beneath Hiawatha Glacier in northwest Greenland. *Science Advances* **4**(11). doi:10.1126/sciadv.aar8173.

Knight PG (1997) The basal ice layer of glaciers and ice sheets. *Quaternary Science Reviews* **16**, 975–993. doi: 10.1016/s0277-3791(97)00033-4.

Koll D and 6 others (2019) Interstellar ^{60}Fe in Antarctica. *Physical Review Letters* **123**(7), 072701. doi:10.1103/PhysRevLett.123.072701.

Kurbatov AV and 22 others (2010) Discovery of a nanodiamond-rich layer in the Greenland Ice Sheet. *Journal of Glaciology* **56**(199), 747–757. doi:10.3189/002214310794457191.

Lalich DE, Holt JW and Smith IB (2019) Radar reflectivity as a proxy for the dust content of individual layers in the Martian north polar layered deposits. *Journal of Geophysical Research Planets* **124**(7), 1690–1703. doi: 10.1029/2018JE005787.

Larsen NK, Kronborg C, Yde JC and Knudsen NT (2010) Debris entrainment by basal freeze-on and thrusting during the 1995–1998 surge of Kuannersuit Glacier on Disko Island, West Greenland. *Earth Surface Processes and Landforms* **16**(B4), 561–574. doi: 10.1002/esp.1945.

Leysinger Vieli GJMC, Martin C, Hindmarsh RCA and Lüthi MP (2018) Basal freeze-on generates complex ice-sheet stratigraphy. *Nature Communications* **9**(1), 1–13. doi: 10.1038/s41467-018-07083-3.

MacGregor JA and 9 others (2015) Radiostratigraphy and age structure of the Greenland Ice Sheet. *Journal of Geophysical Research Earth Surface* **120**(2), 212–241. doi:10.1002/2014JF003215.

MacGregor JA and 6 others (2016*a*) Holocene deceleration of the Greenland Ice Sheet. *Science (New York, N.Y.)* **351**(6273), 590–593. doi:10.1126/science.aab1702.

MacGregor JA and 11 others (2016*b*) A synthesis of the basal thermal state of the Greenland Ice Sheet. *Journal of Geophysical Research Earth Surface* **121** (7), 1328–1350. doi:10.1002/2015JF003803.

McGrath D, Colgan WT, Bayou N, Muto A and Steffen K (2013) Recent warming at summit, Greenland: global context and implications. *Geophysical Research Letters* **40**(10), 2091–2096. doi: 10.1002/grl.50456.

Morlighem M and 31 others (2017) Bedmachine v3: complete Bed topography and ocean bathymetry mapping of Greenland from multibeam echo sounding combined with mass conservation. *Geophysical Research Letters* **44**, 11,051–11,061. doi:10.1002/2017GL074954.

Mouginot J, Bjørk AA, Millan R, Scheuchl B and Rignot EJ (2018) Insights on the surge behavior of Storstrømmen and L. Bistrup Brae, Northeast Greenland, over the last century. *Geophysical Research Letters* **45**, 11197–11205. doi: 10.1029/2018GL079052.

Noël B, van de Berg WJ, Lhermitte S and van den Broeke MR (2019) Rapid ablation zone expansion amplifies north Greenland mass loss. *Science Advances* **5**(9). doi: 10.1126/sciadv.aaw0123.

Pedersen VK, Larsen NK and Egholm DL (2019) The timing of fjord formation and early glaciations in North and Northeast Greenland. *Geology* **47**(7), 682–686. doi: 10.1130/G46064.1.

Petaev MI, Huang S, Jacobsen SB and Zindler A (2013) Large Pt anomaly in the Greenland ice core points to a cataclysm at the onset of Younger Dryas. *Proceedings of the National Academy of Sciences* **110**(32), 12917–12920. doi: 10.1073/pnas.1303924110.

Petrenko VV and 11 others (2009) $^{14}CH_4$ measurements in Greenland ice: investigating last glacial termination CH_4 sources. *Science (New York, N.Y.)* **324**, 506–508. doi:10.1126/science.1168909.

Petrenko VV, Severinghaus JP, Brook EJ, Reeh N and Schaefer H (2006) Gas records from the West Greenland ice margin covering the Last Glacial Termination: a horizontal ice core. *Quaternary Science Reviews* **25**(9–10), 865–875. doi: 10.1016/j.quascirev.2005.09.005.

Porter C and 28 others (2018) ArcticDEM v7, Harvard Dataverse, v1. doi:10.7910/DVN/OHHUKH.

Post A (1972) Periodic surge origin of folded medial moraines on Bering Piedmont Glacier, Alaska. *Journal of Glaciology* **11**(62), 219–226. doi: 10.3189/S0022143000022218.

Putman AL, Fiorella RP, Bowen GJ and Cai X (2019) A global perspective on local meteoric water lines: meta-analytic insight into fundamental controls and practical constraints. *Water Resources Research* **55**(8), 6896–6910. doi: 10.1029/2019WR025181.

Rasmussen, SO and 15 others (2006) A new Greenland ice core chronology for the last glacial termination. *Journal of Geophysical Research* **111**(D6), D06102. doi:10.1029/2005JD006079.

Reeh N, Oerter H and Thomsen HH (2002) Comparison between Greenland ice-margin and ice-core oxygen-18 records. *Annals of Glaciology* **35**, 136–144.

Rhodes RH, Yang X and Wolff EW (2018) Sea ice versus storms: what controls sea salt in arctic ice cores? *Geophysical Research Letters* **45**(11), 5572–5580. doi: 10.1029/2018GL077403.

Risbo T and Pedersen H (1994) Kap York – meteoritekspeditionen. In *Carlsbergfondet Frederiksborgmuseet Ny Carlsbergfondet Ørsskrift*. Copenhagen: RHODOS Internationalt Forlag for Videnskab og Kunst, pp. 38–45.

Ruth U, Wagenbach D, Steffensen JP and Bigler M (2003) Continuous record of microparticle concentration and size distribution in the central Greenland NGRIP ice core during the last glacial period. *Journal of Geophysical Research* **108**(D3), 4098. doi: 10.1029/2002JD002376.

Ryan JC and 7 others (2018) Dark zone of the Greenland Ice Sheet controlled by distributed biologically-active impurities. *Nature Communications* **9**. doi:10.1038/s41467-018-03353-2.

Schaefer H and 6 others (2009) Ice stratigraphy at the Pâkitsoq ice margin, West Greenland, derived from gas records. *Journal of Glaciology* **55**(191), 411–421, doi:10.3189/002214309788816704.

Schäfer JM and 6 others (2000) The oldest ice on Earth in Beacon Valley, Antarctica: new evidence from surface exposure dating. *Earth and Planetary Science Letters* **179**(1), 91–99. doi:10.1016/S0012-821X(00)00095-9.

Sinisalo A and Moore JC (2010) Antarctic blue ice areas – towards extracting palaeoclimate information. *Antarctic Science* **22**(2), 99–115. doi: 10.017/S0954102009990691.

Smith BE and 14 others (2020*a*) Pervasive ice sheet mass loss reflects competing ocean and atmosphere processes. *Science (New York, N.Y.)* **368**(6946), 1239–1242. doi:10.1126/science.aaz5845.

Smith IB and 37 others (2020*b*) The Holy Grail: a road map for unlocking the climate record stored within Mars' polar layered deposits. *Planetary and Space Science* **184**, 104841. doi:10.1016/j.pss.2020.104841.

Steig EJ, Morse DL, Waddington ED and Polissar PJ (1998) Using the sunspot cycle to date ice cores. *Geophysical Research Letters* **25**(2), 163–166. doi: 10.1029/97GL03566.

Tedesco M and Fettweis X (2020) Unprecedented atmospheric conditions (1948–2019) drive the 2019 exceptional melting season over the Greenland ice sheet. *The Cryosphere* **14**, 1209–1223. doi: 10.5194/tc-2019-254.

Wientjes IGM and 5 others (2012) Carbonaceous particles reveal that Late Holocene dust causes the dark region in the western ablation zone of the Greenland ice sheet. *Journal of Glaciology* **58**(210), 787–794. doi: 10.3189/2012JoG11J165.

Winter, K and 10 others (2016) Assessing the continuity of the blue ice climate record at Patriot Hills, Horseshoe Valley, West Antarctica. *Geophysical Research Letters* **43**(5), 2019–2026. doi:10.1002/2015GL066476.

Yan Y and 10 others (2019) Two-million-year-old snapshots of atmospheric gases from Antarctic ice. *Nature* **574**, 663–666. doi:10.1038/s41586-019-1692-3.

Yang K and 6 others (2019) Supraglacial rivers on the northwest Greenland Ice Sheet, Devon Ice Cap, and Barnes Ice Cap mapped using Sentinel-2 imagery. *International Journal of Applied Earth Observation and Geoinformation* **78**, 1–13. doi: 10.1016/j.jag.2019.01.008.

Zwally HJ, Giovinetto MB, Beckley MA and Saba JL (2012) Antarctic and Greenland drainage systems. Available at http://icesat4.gsfc.nasa.gov/cryo_data/ant_grn_drainage_systems.php.

Appendix A

Animations

See Figures 12–14.

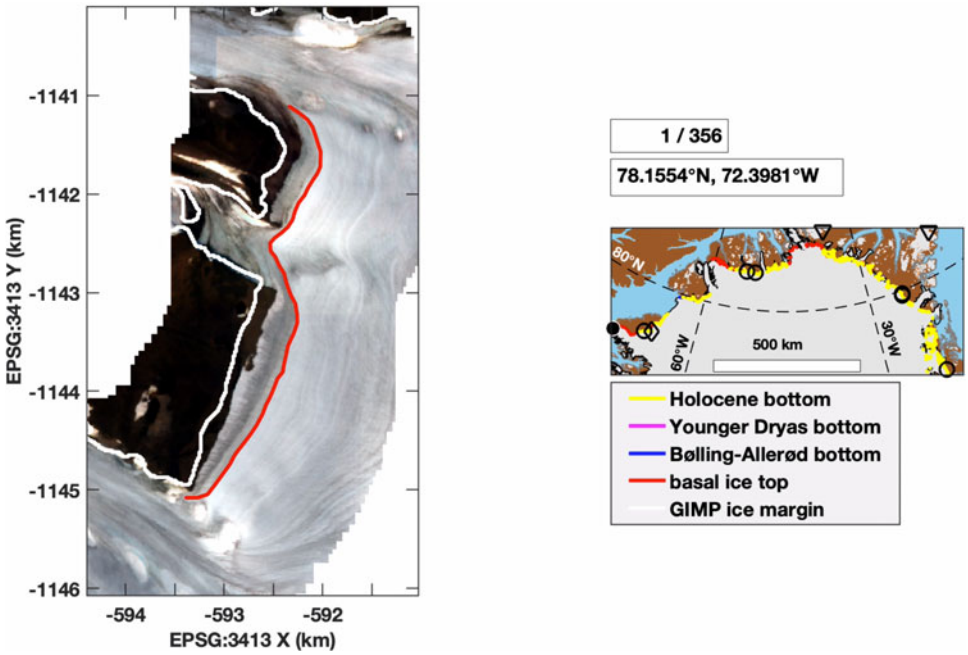

Fig. 12. Snapshot of Supplementary File 3. All traced boundary segments showed sequentially, clockwise about northern Greenland. A sub-scene of the S2 mosaic is generated for each digitised point with a 1-km buffer, then contrast-stretched to emphasise margin stratigraphy. Note that the scale for each frame varies depending on segment length, but that it is typically larger than that at which we traced boundaries in the imagery (1: 10 000). Contains Copernicus Sentinel-2 2019 data processed by ESA.

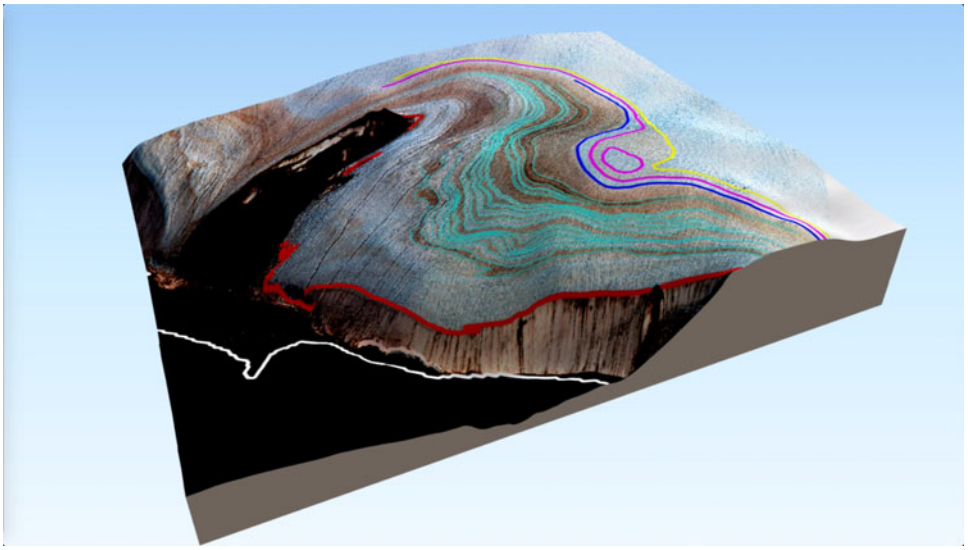

Fig. 13. Snapshot of Supplementary File 4. A rotation about a 3-D representation of Fig. 10a, i.e. the same WV subscene draped over ArcticDEM. Vertical exaggeration is 5x. WV imagery is copyright 2020 DigitalGlobe Inc.

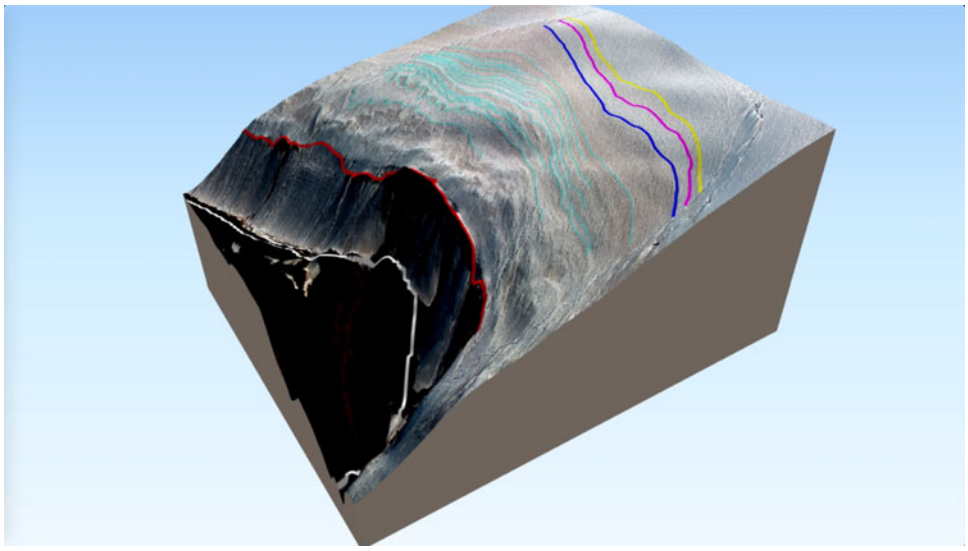

Fig. 14. Snapshot of Supplementary File 5. Same as Fig. 13 but showing the same region as Fig. 10b. WV imagery is copyright 2020 DigitalGlobe Inc.